FACULDADE DE ENGENHARIA DA UNIVERSIDADE DO PORTO

UPWIND- Development of a Take-off and Landing Platform for Integration in an Airborne Wind Energy System

Pedro João Moreira Cruz Peixoto

Mestrado em Engenharia Eletrotécnica e de Computadores

Supervisor: Prof. Dr. Fernando Arménio da Costa Castro e Fontes

July 30, 2026

© Pedro João Peixoto, 2026

Resumo

Os Sistemas Aéreos de Energia Eólica (AWES, sigla em inglês) representam uma fronteira promissora na produção de energia sustentável, sendo capazes de aproveitar ventos a grande altitude, inacessíveis às turbinas eólicas convencionais. O projeto UPWIND, desenvolvido na Universidade do Porto, foca-se numa configuração de geração no solo, onde a energia é extraída através da tensão do cabo numa arquitetura de ciclo de bombeamento. Embora tenham sido feitos progressos significativos na modelação e na maximização de potência, a automação da descolagem e aterragem continua a ser um elo em falta crítico para a operação autónoma de ciclo completo. Este trabalho aborda esta lacuna através do desenvolvimento de uma estratégia de controlo de sincronização e captura para uma plataforma de Descolagem e Aterragem Automáticas (ATOL, sigla em inglês), baseada numa arquitetura de Descolagem e Aterragem Circular (CTOL, sigla em inglês), na qual um carro no solo segue o movimento azimutal de uma aeronave amarrada ao longo de uma pista circular.

É formulado um modelo cinemático e dinâmico acoplado do sistema kite-carro, sendo projetada uma arquitetura de controlo hierárquico, que combina uma lei de sincronização baseada em Kuramoto com estratégias de controlo específicas para cada fase, de modo a coordenar o sistema ao longo de todas as fases da missão autónoma.

A estratégia proposta é primeiramente validada através de simulação numérica em MATLAB, demonstrando a convergência dos erros de seguimento angular e de velocidade para valores dentro das tolerâncias exigidas para uma captura segura e automatizada. Para colmatar a lacuna entre a modelação teórica e a implementação física, foi desenvolvido um protótipo de hardware do carro no solo, o qual foi validado através de uma configuração hardware-in-the-loop (HIL), na qual um sinal simulado da aeronave, gerado por um microcontrolador dedicado, foi utilizado para testar o desempenho de seguimento em tempo real do carro sob a fase de loitering (altitude constante) da missão. Embora a validação completa com uma aeronave física em voo permaneça como trabalho futuro, os resultados obtidos fornecem uma base robusta para o desenvolvimento contínuo de capacidades ATOL totalmente autónomas no âmbito do projeto UPWIND.

Abstract

Airborne Wind Energy Systems (AWES) represent a promising frontier in sustainable power generation, capable of harvesting high-altitude winds inaccessible to conventional wind turbines. The UPWIND project, developed at the University of Porto, focuses on a ground-generation configuration, where energy is extracted through tether tension in a pumping-cycle architecture. While significant progress has been made in modeling and power maximization, the automation of launch and recovery remains a critical missing link for full-cycle autonomous operation.

This work addresses this gap by developing a synchronization and capture control strategy for an Automatic Take-off and Landing (ATOL) platform, based on a Circular Take-off and Landing (CTOL) architecture in which a ground-based cart tracks the azimuthal motion of a tethered aircraft along a circular track. A coupled kinematic and dynamic model of the kite-cart system is formulated, and a hierarchical control architecture, combining a synchronization law with phase-specific control strategies, is designed to coordinate the system throughout all phases of the autonomous mission.

The proposed strategy is first validated through numerical simulation in MATLAB, demonstrating convergence of the angular and velocity tracking errors to within the tolerances required for a safe, automated capture. To bridge the gap between theoretical modeling and physical implementation, a hardware prototype of the ground-based cart was developed and validated through a hardware-in-the-loop setup, in which an emulated aircraft signal, generated by a dedicated microcontroller, was used to test the cart's real-time tracking performance under the constant-altitude loitering phase of the mission. While full validation with a physically flying aircraft remains for future work, the results obtained provide a robust foundation for the continued development of fully ATOL capabilities for AWES.

UN Sustainable Development Goals

Adopted by all Member States of the United Nations in 2015, the 2030 Agenda for sustainable Development sets out a common framework to promote peace and prosperity for people and the planet. The 17 Sustainable Development Goals represent an urgent call to action for all countries, developed and developing, through a global partnership [1].

Airborne Wind Energy Systems represent an innovative renewable energy technology that perfectly aligns with some of the UN Sustainable Development Goals. Since these systems harness stronger and more consistent winds at higher altitudes, using tethered flying devices, AWES can generate electricity with reduced material and minimal environmental impact, compared to the traditional and heavy wind turbines.

Hence, the Sustainable Development Goals associated to AWES are the following:

SDG 7: Ensure access to affordable, reliable, sustainable and modern energy for all.

SDG 9: Build resilient infrastructure, promote inclusive and sustainable industrialization, and foster innovation.

SDG 11: Make cities and human settlements inclusive, safe, resilient and sustainable.

SDG 13: Take urgent action to combat climate change and its impacts.

Table 1: UN Sustainable Development Goals (Contributions and Performance Indicators)

SDG	**Target**	**Contribution**	**Performance Indicators and Metrics**
7	7.1	The performance of autonomous control algorithms, enables the deployment of AWES as a mobile energy solution	Indicator 7.1.2: Proportion of population with primary reliance on clean fuels and technology.
	7.2	Development of autonomous control for high-altitude wind harvesting, accessing wind speeds typically unavailable to conventional turbines.	Indicator 7.2.1: Increase in renewable energy capacity factor; reduction in Levelized Cost of Energy (LCOE) for AWES.
9	9.2	By lowering the technical and capital barriers to renewable energy production, this research shifts toward inclusive industrialization.	Indicator 9.2.1: Manufacturing value added as a proportion of GDP and per capita.
	9.4	Engineering a system with significantly reduced material intensity (replacing steel towers with intelligent flight control).	Indicator 9.4.1: CO2 footprint per kWh produced; ratio of material weight to rated power (kg/MW).
11	11.a	AWES provide a highly compact footprint, eliminating the massive concrete foundations and heavy tower structures of conventional wind turbines. This allows for land-use maximization and the potential integration of clean energy generation near peri-urban communities or microgrids, fostering sustainable regional development with minimal environmental and visual disruption.	Indicator 11.a.1: Number of countries that have national urban policies or regional development plans that respond to population dynamics, ensure balanced territorial development and increase local fiscal space.
	11.b	The compact and portable nature of small-scale AWES makes them ideal for rapid deployment in disaster-stricken areas or isolated human settlements. By providing a resilient, infrastructure-light, and autonomous source of high-altitude wind power, the system enhances the energetic resilience of communities against climate-induced grid failures.	Indicator 11.a.2: Proportion of local governments that adopt and implement local disaster risk reduction strategies in line with national disaster risk reduction strategies.
13	13.1	Enabling rapid deployment of mobile wind units to strengthen energy resilience in remote areas or disaster-hit regions.	Indicator 13.1.1: Ensuring continuous power for emergency response and medical facilities in disaster zones.
	13.2	By providing a validated Python-based framework for state-space control and trajectory optimization, this research enables energy planners to accurately quantify the decarbonization potential of AWES.	Indicator 13.2.1: Integration of AWES performance data into decarbonization roadmaps.

Acknowledgements

I would like to express my sincere gratitude to my supervisor Professor Fernando A. C. C. Fontes, for the invaluable guidance, continuous support and patience during this academic year. Their immense knowledge and insightful feedback were fundamental to the successful completion of this Dissertation.

I am also deeply thankful to all the members of the UPWIND team for creating such a welcoming, collaborative and motivating environment, in particular to Sérgio Vinha and João Fernandes for their support and assistance.

On a personal note, I would like to express my deepest appreciation to my Family for their unconditional love, continuous encouragement and for being my ultimate support system throughout these past five years. Everything I have achieved is thanks to them.

A special thank you goes to the friends who made this academic journey unforgettable. To the "Engenheiros Aspirantes" group, my housemates from Xior – in particular the "7º+Infiltrados" group – and my lifelong friends from Externato, thank you for your friendship, which I know will last a lifetime. I also cherish the memories and the incredible people I met during my Erasmus exchange in Belgium which truly helped me grow and change my perspective on the world.

To everyone who shared dinners, road trips, holidays, "Queima das Fitas" and all the good moments with me, thank you for making these years at FEUP so special, I will remember them for the rest of my life.

Pedro João M. C. Peixoto

"Kites rise highest against the wind, not with it"

Winston Churchill

Contents

1 Introduction **1**
- 1.1 Context and Motivation . . . 1
- 1.2 Objectives and Problem Definition . . . 3
- 1.3 Contributions . . . 3
- 1.4 Dissertation Structure . . . 4

2 Airborne Wind Energy Systems **5**
- 2.1 Historical Background . . . 5
- 2.2 Basic Concepts and Crosswind Kite Power . . . 7
- 2.3 Classification of AWES . . . 9
- 2.4 Automatic Take-off and Landing . . . 11
  - 2.4.1 Vertical Take-off and Landing (VTOL) . . . 12
  - 2.4.2 Horizontal Take-off and Landing (HTOL) . . . 14
  - 2.4.3 Circular Take-off and Landing (CTOL) . . . 15
- 2.5 UPWIND Project . . . 17

3 Kite-Cart System Dynamics **19**
- 3.1 Coordinate Frames . . . 19
- 3.2 Rotation Matrices . . . 21
- 3.3 Tethered Aircraft Kinematics . . . 22
- 3.4 Actuating Forces . . . 24
- 3.5 Kite Model . . . 25
- 3.6 Cart Model . . . 26

4 Synchronization of Kite-Cart System for Circular Landing **28**
- 4.1 Control Architecture . . . 28
- 4.2 Kite Control Laws . . . 29
- 4.3 Cart Control Law . . . 30
- 4.4 Autonomous Capture Strategy . . . 31
- 4.5 Simulation Results . . . 32

5 Hardware Implementation **37**
- 5.1 Experimental Implementation . . . 37
- 5.2 Hardware Architecture . . . 40
  - 5.2.1 Kite Subsystem . . . 40
  - 5.2.2 Cart Subsystem . . . 42
- 5.3 Software Implementation . . . 48
- 5.4 Experimental Validation . . . 49

5.5 Discussion 57

6 Conclusion **59**
6.1 Future Work 60

References **61**

List of Figures

1.1 Comparison Between Traditional Wind Turbines (Left) and AWES (Right). (Source: [5]) . . . 2

2.1 Number of Institutions involved in AWES. (Source: [8]) . . . 6
2.2 Institutions and Companies working in AWES. (Source: [12]) . . . 6
2.3 Traditional Wind Turbine (Left) and Flying Wing (Right). (Source: [10]) . . . 7
2.4 AWES Examples: a) Ground Generation and b) Onboard Generation. (Source: [9]) 8
2.5 AWES Diversity Classification. (Source: [16]) . . . 10
2.6 Kite Flight Path (Left) and Instantaneous Mechanical Power Output for a Ground-Generation AWES (Right). (Source: [8]) . . . 10
2.7 Different Types of Energy Conversion. (Source: [17]) . . . 11
2.8 Makani Power VTOL Prototype. (Source: [24]) . . . 12
2.9 KiteMill VTOL Prototype. (Source: [4]) . . . 13
2.10 TwingTec VTOL Prototype. (Source: [9]) . . . 14
2.11 Ampyx Power HTOL Prototype. (Source: [25]) . . . 15
2.12 ElektRail HTOL Prototype. (Source: [27]) . . . 15
2.13 Experimental CTOL. (Source: [9]) . . . 16
2.14 EnerKite Rotational Arm. (Source: [4]) . . . 17
2.15 UPWIND Aircraft Prototype. (Source: [9]) . . . 18

3.1 Body Frame (Coordinate System): Top and Side Views. . . . 20
3.2 Global and Local Frames and Tangent Plane τ at Position p. (Source: Adapted from [4]) . . . 20
3.3 2D Rotation Frames. (Source: [28]) . . . 21
3.4 Circular Take-off Trajectory. (Source: [18]) . . . 22
3.5 Aircraft Longitudinal Model. (Source: [18]) . . . 23

4.1 State Machine Describing the Flight Phases: Take-Off (Light Yellow), Loiter (Light Green) and Landing (Light Blue). (Source: [18]) . . . 29
4.2 Flight Phases in MATLAB (P1-P4). . . . 33
4.3 Flight Phases in MATLAB (P5-P8). . . . 33
4.4 Angular Error of the Kite-Cart System (P1-P4). . . . 34
4.5 Angular Error of the Kite-Cart System (P4-P8). . . . 34
4.6 Linear Velocity Error of the Kite-Cart System (P1-P4). . . . 35
4.7 Linear Velocity Error of the Kite-Cart System (P4-P8). . . . 35
4.8 Control Inputs Evolution of the Kite-Cart System (P1-P4). . . . 36
4.9 Control Inputs Evolution of the Kite-Cart System (P4-P8). . . . 36

5.1 Experimental setup showing the tethered cart on the ground connected to the central anchorage point (Tether Highlighted in Blue). 38
5.2 WiFi Communication Configuration. 39
5.3 Cart Setup Connections. 40
5.4 Arduino 33 IoT. 41
5.5 Arduino 33 IoT Pinout. (Source: [30]) 42
5.6 Raspberry Pi Pico 2W. 43
5.7 Raspberry Pi Pico 2W Pinout. (Source: [31]) 43
5.8 IMU BNO085. 44
5.9 MicroSD Card Module for Data Logging. 45
5.10 L298N Motor Driver. (Source: [32]) 46
5.11 Power Supply. 47
5.12 Cart Setup. 48
5.13 Software Implementation Flowchart. 49
5.14 Synchronization Results (Transient): Configuration A. 51
5.15 Synchronization Results (Steady-State): Configuration A. 51
5.16 Synchronization Results (Transient): Configuration B. 53
5.17 Synchronization Results (Steady-State): Configuration B. 53
5.18 Synchronization Results (Transient): Configuration C. 54
5.19 Synchronization Results (Steady-State): Configuration C. 55
5.20 Synchronization Results (Transient): Configuration D. 56
5.21 Synchronization Results (Steady-State): Configuration D. 57

List of Tables

1 UN Sustainable Development Goals (Contributions and Performance Indicators) . iv

4.1 Simulation Parameters and Controller Gains. 30

5.1 Controller Gains: All Configurations 50
5.2 Controller Gains: Configuration A 50
5.3 Controller Gains: Configuration B 52
5.4 Controller Gains: Configuration C 54
5.5 Controller Gains: Configuration D 55

List of Acronyms

AWES	Airborne Wind Energy Systems
ATOL	Automatic Take-off and Landing
TOL	Take-off and Landing
CTOL	Circular Take-off and Landing
HTOL	Horizontal Take-off and Landing
VTOL	Vertical Take-off and Landing
HAWT	Horizontal-Axis Wind Turbine
UAV	Unmanned Aerial Vehicle
MPC	Model Predictive Control
PID	Proportional-Integral-Derivative
LQR	Linear Quadratic Regulator
RF	Radio-Frequency
UDP	User Datagram Protocol
IMU	Inertial Measurement Unit
SPI	Serial Peripheral Interface
I2C	Inter-Integrated Circuit
GPIO	General-Purpose Input/Output
PWM	Pulse-Width Modulation
SDG	Sustainable Development Goal

Chapter 1

Introduction

This chapter begins with the context and motivation that instigates the necessity of harvesting stable and high-altitude winds. The core objectives of this research are also specified according to the operational challenges of implementing an Automatic Take-Off and Landing platform for Airborne Wind Energy Systems. Lastly, the structure of the dissertation is outlined.

1.1 Context and Motivation

Driven by the dual imperatives of mitigating anthropogenic climate change and addressing depleting fossil fuel reserves, renewable energy has moved to the forefront of the global energy agenda. Consequently, the renewable energy sector has expanded rapidly, outpacing traditional power generation over the past several decades [2]. Electricity is a fundamental prerequisite for the delivery of vital public services, ranging from education to healthcare systems. While fossil and nuclear energy have historically powered these sectors, they are increasingly characterized by sustainability deficits. These include environmental degradation and volatility in supply and pricing, necessitating a transition toward more resilient and sustainable energy architectures [3].

Renewable sources serve as the central drivers of the energy transition due to their environmental sustainability and vast potential for further development. Driven by this shift, renewable production is forecasted to outpace fossil-fuel generation by 2035. The deployment of high efficiency systems capable of harvesting untapped resources will be needed [4]. In the current energy landscape, on-shore wind turbines are the dominant modality for large-scale production, with hub heights typically ranging from 50 to 300 meters. However, the scalability of this technology is constrained by its inability to access the superior wind regimes found at higher altitudes [5]. This leaves a significant portion of the global wind resource unexploited.

High-altitude winds offer a more stable and potent energy resource compared to the intermittent flows found near the surface. While increasing the hub height and rotor diameter of traditional turbines is a theoretical possibility, the logistical and structural costs of such massive

towers are economically unsustainable [5]. This creates a clear market demand for more efficient, infrastructure-light solutions that can access high-altitude winds, ensuring that wind power remains a sustainable component of the global energy mix.

A prominent innovation in the search for this untapped resource is Airborne Wind Energy (AWE), an emerging field that targets energy extraction at high altitudes. The operational units within this sector, known as Airborne Wind Energy Systems (AWES), replace the heavy infrastructure of towers with aerodynamically efficient tethered wings [6]. They occupy less space and weight less, for the same power output (see Figure 1.1).

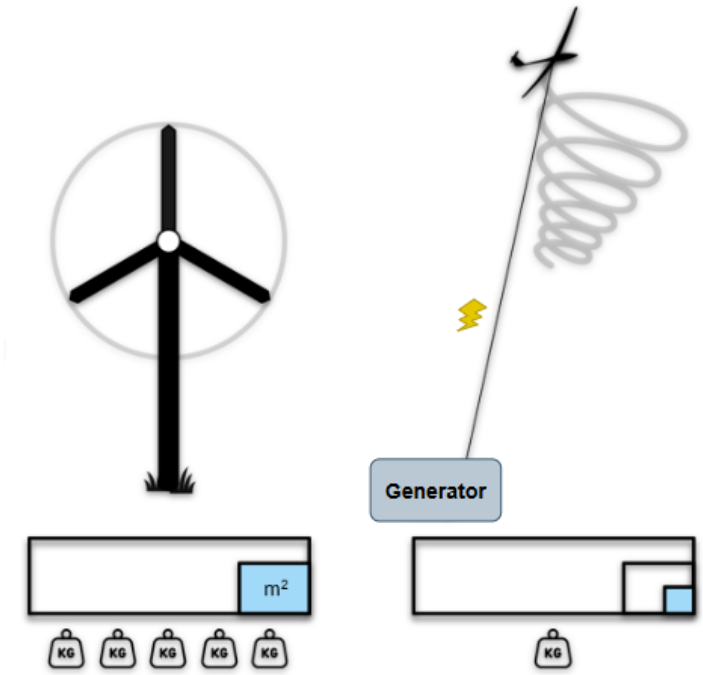

Figure 1.1: Comparison Between Traditional Wind Turbines (Left) and AWES (Right). (Source: [5])

One of the most promising paradigms within AWES involves a controlled aerodynamic wing connected to a generator via a high-strength tether. These systems leverage crosswind flight, moving almost perpendicular to the wind direction, to sweep an operational area significantly larger than that of conventional turbine blades. Optimal energy extraction is achieved when the wing maintains a periodic trajectory, typically characterized by elliptical or figure-eight patterns. However, the precise execution of these flight paths remains a significant control challenge. As the technology has yet to reach full maturity, there exists a critical research frontier for developing more robust control methodologies and innovative hardware solutions.

A key enabler of this technology lies in the ability to operate autonomously over long periods

and under a wide range of weather conditions, with minimal human intervention. Achieving this level of autonomy is critical to ensuring the operational viability of AWES, as any system that still relies on manual Take-Off and Landing cannot be deployed at scale. Nevertheless, the development of Automatic Take-off and Landing (ATOL) capabilities is a necessary condition for the technology to mature beyond the experimental stage.

1.2 Objectives and Problem Definition

Automatic Take-off and Landing (ATOL) represents one of the most significant technical hurdles preventing tethered wing technology from achieving full commercial maturity, as autonomous operation throughout the entire flight envelope is a prerequisite for unattended large-scale deployment. Within this context, the main objective of this work is to design, model and implement an ATOL platform tailored to the small-scale aircraft prototype of the UPWIND project.

More specifically, the objective of this work aims to formulate a coupled kinematic and dynamic model capturing the multi-body interaction between the airborne kite and a ground-based tracking cart constrained to a circular trajectory, design a hierarchical control architecture capable of synchronizing the angular position and velocity of the cart with those of the kite throughout all phases of the autonomous mission, from initial acceleration to final capture.

Finally validate the proposed control strategy through numerical simulation, assessing its ability to maintain angular and velocity tracking errors within the tolerances required for a safe, automated landing approach. Then the design and implementation of a dedicated embedded hardware architecture, comprising the kite and cart subsystems, their sensing, actuation, and wireless communication infrastructure, capable of physically realizing the proposed control strategy on a representative testbed.

The central technical challenge underlying this work lies in coordinating two physically distinct subsystems, a freely flying tethered wing and a ground auxiliary vehicle, under a shared circular trajectory, while accounting for the constraints of the cart and the communication latency inherent to a distributed, wireless control architecture. Addressing this challenge requires bridging theoretical control design with practical hardware implementation, ensuring that the resulting framework can serve as a major step toward a fully autonomous, flight-tested ATOL system.

1.3 Contributions

By leveraging an established Ground Generation infrastructure and a pre-characterized aircraft prototype, this project did not need to build a system entirely from scratch. Instead, it contributes a critical missing component to the UPWIND project, an Automatic Take-Off and Landing platform. The primary research and engineering outputs developed in the scope of this dissertation represent direct advancements for the ATOL capabilities of the UPWIND research project platform. The main contributions of this work are summarized as follows:

- **Scientific Publication:** The theoretical and mathematical foundations established in this research culminated in the publication of a peer-reviewed scientific paper entitled *"Synchronization and Capture Control of a Kite-Cart System for Tethered Circular Landing"* at the 17TH APCA International Conference on Automatic Control and Soft Computing, Coimbra 2026 [7].
- **Coupled Kinematic Modeling:** Formulation of a mathematical framework mapping the multi-body dynamic constraints between the kite subsystem and the cart subsystem, constrained to a circular track.
- **Hierarchical Synchronization Control Setup:** Design and numerical validation of a control architecture for angular synchronization, coordinating the ground auxiliary cart with the kite's circular flight path throughout all flight phases.
- **Hardware Integration:** Complete architectural specification, structural planning and hardware integration of an autonomous auxiliary ground cart built around a main microcontroller and validated through a hardware-in-the-loop setup using a second microcontroller for real-time wireless emulation of the flight behaviour of the kite.

1.4 Dissertation Structure

This dissertation is divided into six chapters, initiating from the fundamental theoretical concepts to the hardware implementation and experimental validation. Chapter 2 provides the AWES literature review and the state of the art. It introduces the historical background, basic concepts of crosswind kite power, followed by the assessment of the classification of AWES and details about Automatic Take-Off and Landing. It finishes with the contextualization of the UPWIND project, which presents the Kite-Cart system that will be the core of this work. Chapter 3 is entirely dedicated to the dynamical and kinematic modeling of the coupled system, presenting the necessary coordinate frames, rotation matrices, aerodynamic and tether forces acting on the system. Then the respective state-space representation is formalized for both kite and cart.

Chapter 4 focuses on the Kite-Cart system synchronization for tethered circular landing, describing the overview of the hierarchical control architecture, presenting the control laws implemented for both vehicles, concluding with the autonomous capture logic. Chapter 5 encompasses the practical execution and validation of the implemented control algorithms. It starts by showing the hardware used for each subsystem, its physical implementation, ending with the analysis and validation of the obtained experimental results. Chapter 6 summarizes the main contributions of this research and proposes directions for future work.

Chapter 2

Airborne Wind Energy Systems

This chapter provides a comprehensive literature review and State-of-the-Art in Airborne Wind Energy Systems, establishing the theoretical and contextual foundation necessary to understand the dynamics and control challenges addressed in this work.

2.1 Historical Background

At the end of the Industrial Revolution, when George Pocock published the book "The Aeropleustic Art or Navigation in the Air by the use of Kites, or Buoyant Sails", the earliest research concerning AWES can be traced back to 1827. From the very beginning, early civilizations explored different techniques for maneuvering and controlling cloth-covering wings, enabling them to capture and use wind energy. In the 1930s, Hermann Honnef, a German engineer and settler in wind energy, proposed concepts for large-scale wind power plants featuring multiple rotors mounted on towers, reaching some hundred meters in height [8]. Concurrently, another German engineer, Aloys van Gries introduced the combination of large lifter kites, widely used by observatories around the world for high altitude measurements.

Approximately four decades later, during the energy crisis of the 1970s, when the use of fossil fuels and nuclear power was a major problem, there has been a growing need to use natural resources to produce energy [9]. Addressing this challenge, Hermann Oberth presented the harvesting of high altitude winds as a possible alternative to traditional power generation.

Building on this concept, the idea of capturing energy from tethered airfoils racing across the wind was first explored in depth by Miles Loyd. During the 1970s and 80s, the American engineer laid the theoretical groundwork for modern airborne wind technology [10], introducing the mathematical framework that would later underpin the field of Crosswind Kite Power. Although the conventional three-bladed horizontal-axis wind turbine (HAWT) has remained the dominant paradigm for utility-scale wind power generation over the past forty years, contemporary research and industrial innovation are increasingly shifting toward Airborne Wind Energy Systems [9]. This paradigm shift is evidenced by an expanding body of research across prominent international

academic and corporate institutions, driven by the goal of harvesting the stronger and more consistent wind resources available at high altitude, and developing highly scalable, sustainable energy solutions. Figure 2.1 illustrates the increasing global interest in AWES, showing a significant rise in the number of institutions involved in this research field between 2000 and 2018.

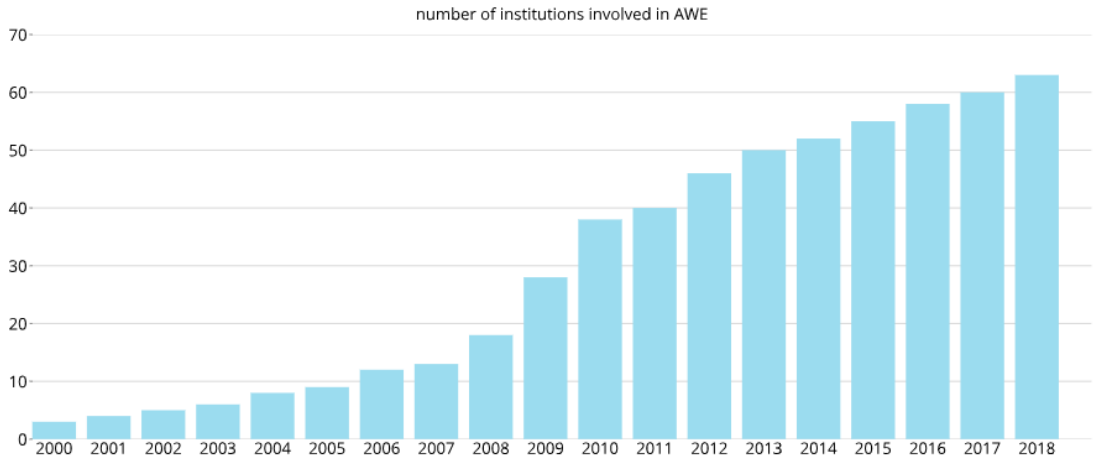

Figure 2.1: Number of Institutions involved in AWES. (Source: [8])

For the purpose of this count, entities involved in AWES Research and Development (R&D) are strictly limited to academic groups and commercial teams actively working on complete systems. By 2025, the Research & Development (R&D) field was composed of more than 60 institutions, including Academia institutions, Government entities and Companies, as clearly represented in Figure 2.2. This growing institutional engagement is also reflected at the conference level: in 2026, the University of Porto hosted the 11th International Airborne Wind Energy Conference (AWEC 2026), jointly organized with Airborne Wind Europe and Delft University of Technology, bringing together many of the research groups and companies identified in Figure 2.2 [11].

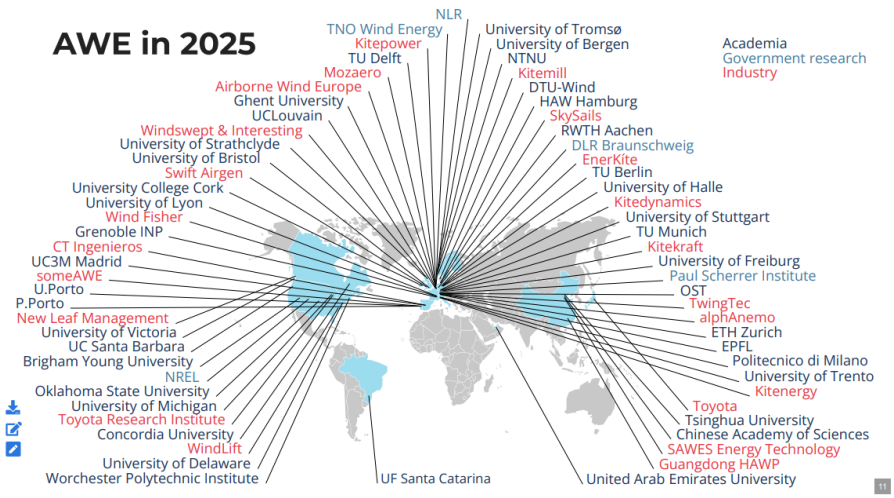

Figure 2.2: Institutions and Companies working in AWES. (Source: [12])

2.2 Basic Concepts and Crosswind Kite Power

As introduced in Section 2.1, this concept of generating power with tethered aircraft flying at high speed in the crosswind direction was deeply investigated during the 1970s and 1980s by Miles Loyd, who was arguably the first to formally compute the power generation potential of fast-flying tethered wings [13]. Loyd identified the blade tips as the most aerodynamically efficient region of a wind turbine due to their larger interaction within an effective wind area. Loyd also investigated, and later patented, the idea of using an aircraft or kite flying in closed-loop trajectories while tethered to the ground. Two methods for converting this concentrated form of wind power into useful energy were proposed by him: Lift mode and Drag mode, illustrated in Figure 2.3 and detailed below.

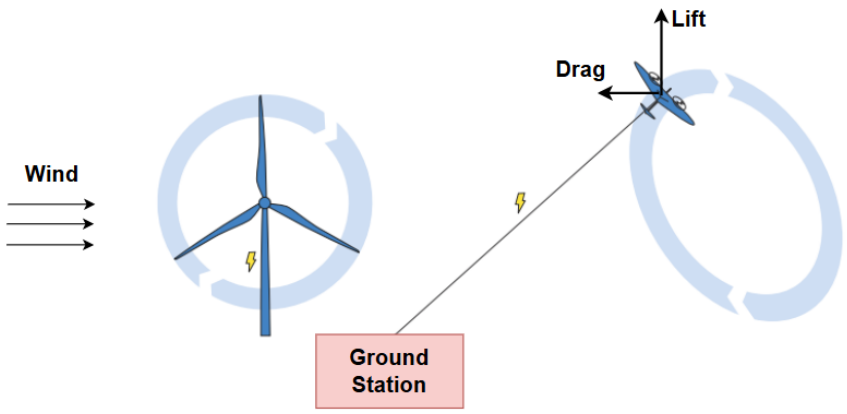

Figure 2.3: Traditional Wind Turbine (Left) and Flying Wing (Right). (Source: [10])

In Lift mode, energy is extracted through tether tension acting on a ground load, while in Drag mode, the elevated apparent airspeed is used to drive an onboard wind turbine. As stated in [10], Loyd derived an approximate expression for the power generation P, produced by a tethered airfoil operating either in Lift or Drag mode. The expression is given by

$$P = \frac{2}{27}\rho A v_w^3 C_L \left(\frac{C_L}{C_D}\right)^2, \tag{2.1}$$

where A denotes the wing area, C_L and C_D the Lift and Drag coefficients, ρ represents the air density, v_w the wind speed and the ratio $\left(\frac{C_L}{C_D}\right)^2$, the wing property which is a crucial indicator of aerodynamic efficiency under specific flight conditions [10]. Loyd further determined the maximum mechanical power that an aircraft tethered to the ground can extract from a wind field. Under idealized assumptions [14], the maximum power output $P_{\max}$ is given by

$$P_{\max} \leq \frac{2}{27}\rho A v_w^3 C_L \left(\frac{C_L}{C_D}\right)^2 \cos^3\gamma. \tag{2.2}$$

This extends Equation 2.1 by introducing $cos^3\gamma$ term and using the same variables stated in Equation 2.1, representing the maximum power output that an aircraft can produce. The angle γ *is the angle between the wind velocity vector and the vector that points along a straight tether from the attachment point on the ground to the aircraft* [14].

AWES present a different approach to power generation. Instead of relying on traditional and heavy wind turbines, AWES *are connected by a tether to the ground, like kites or tethered balloons* [10], operating through a mechanical tether to the ground, which allows them to harness wind energy. These systems *can be connected to a stationary ground station*, as power can be produced in the form of a traction force *to a moving vehicle, or in form of electricity* [10].

The motivation behind the development of these systems is threefold. First, wind power, alongside solar energy, represents some of the renewable resources large enough to meet the global humanity energy demand. Second, as mentioned in Section 2.1, unlike conventional and heavy wind turbines, AWES are designed to access significantly higher altitudes, tapping into a massive and largely unexploited wind resource. Third and most important, AWES require less material investment compared to other conventional technologies, having a favorable high power to mass ratio [10]. Figure 2.4 displays the two primary operating principles of AWES: Ground Generation and Onboard Generation. The UPWIND project specifically adopts the Ground Generation configuration, where mechanical power is produced on the ground through the tether traction.

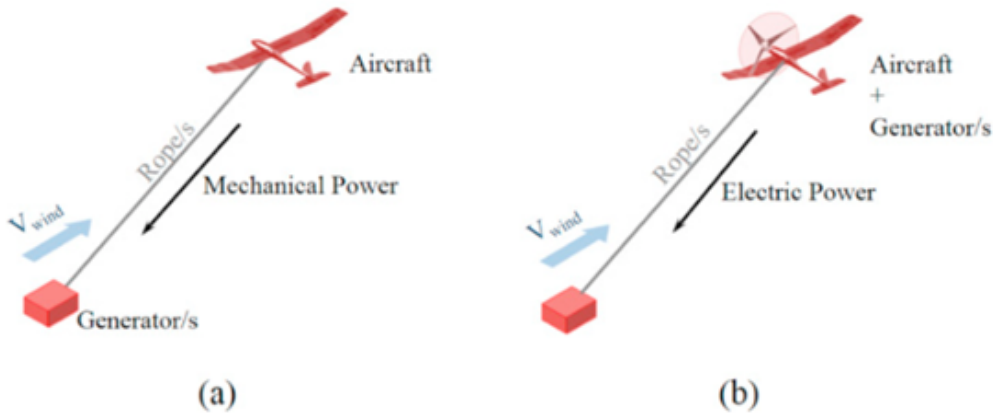

Figure 2.4: AWES Examples: a) Ground Generation and b) Onboard Generation. (Source: [9])

According to [15] and [10], in Ground Generation systems, the aircraft remains purely passive in terms of energy conversion, as it flies under aerodynamic forces and these forces are transmitted through the tether to a ground station, where a generator converts the tether's traction into electricity. This configuration allows the airborne component to remain lightweight, since no generator or power electronics need to be carried aloft. This is the most common configuration among AWES, often referred to as the *pumping* or *yo-yo* method, due to its intermittent generation pattern. In this approach, the aircraft is tethered to a fixed point on the ground and the kinetic energy captured

from the wind generates a pulling force that unreels the tether from a drum connected to a generator. The operation cycle is composed of two distinct phases: a traction (or reel-out) phase, during which the tether extends and electrical energy is produced, and a recovery (or reel-in) phase, in which a smaller amount of energy is consumed to retract the airborne element to a lower altitude, preparing it for the next cycle. During the traction phase, the flight path is actively controlled to exploit crosswind motion, maximizing the energy produced, while during recovery, the trajectory is adjusted to minimize the energy consumed in pulling the tether back in. Typically, the aircraft follows a figure-eight flight pattern, or a circle.

In Onboard Generation systems, by contrast, the generator is mounted directly on the flying device. Onboard-generating devices are also tethered to the ground at a fixed location, but unlike Ground Generation, the tether length remains fixed during normal operation. Instead of transmitting mechanical traction to the ground, the power conversion equipment is carried onboard the aircraft, where one or more rotors drive onboard generators directly. The resulting electrical power is then transmitted back to the base station through the tether itself, which must therefore be electrically conducting. To maximize energy capture, the airborne element flies crosswind to augment the apparent wind inflow, typically following either a circular or a figure-eight trajectory [15].

A simple observation familiar to any kite surfer or hobby kite pilot illustrates the core principle behind crosswind kite power, as soon as a kite flies fast loops across the wind direction, the tension on the lines increases sharply, to the point where hobby pilots must actively compensate for it by hand [13]. This happens because the aerodynamic lift force generated by a wing grows with the square of its apparent airspeed v_a that is, the speed of the wing relative to the surrounding air, rather than with the ambient wind speed v_w itself. As a direct consequence, flying a kite crosswind at an apparent speed just ten times greater than the wind speed increases the tether tension by a factor of one hundred, compared to a kite held stationary in the sky.

2.3 Classification of AWES

The diversity of AWES technologies can be better understood through a systematic categorization of existing architectures. Figure 2.5 illustrates this classification based on electricity generation methods and flight operation modes. Building on the Ground and Onboard Generation principles introduced in Section 2.2, the highest level of AWES categorization differentiates systems based on the type of ground station (fixed or moving), or, in the case of Onboard Generation, the use of a conducting tether [8]. At a second level, systems are categorized according to their flight operation mode. Three primary patterns are identified: crosswind flight, tether-aligned flight, which lacks a significant crosswind component, and the rotational operation of the entire device. While both crosswind and tether-aligned configurations are characterized by the transfer of tensile pulling forces to the ground station, rotational systems are distinguished by the transmission of an additional torque component [8].

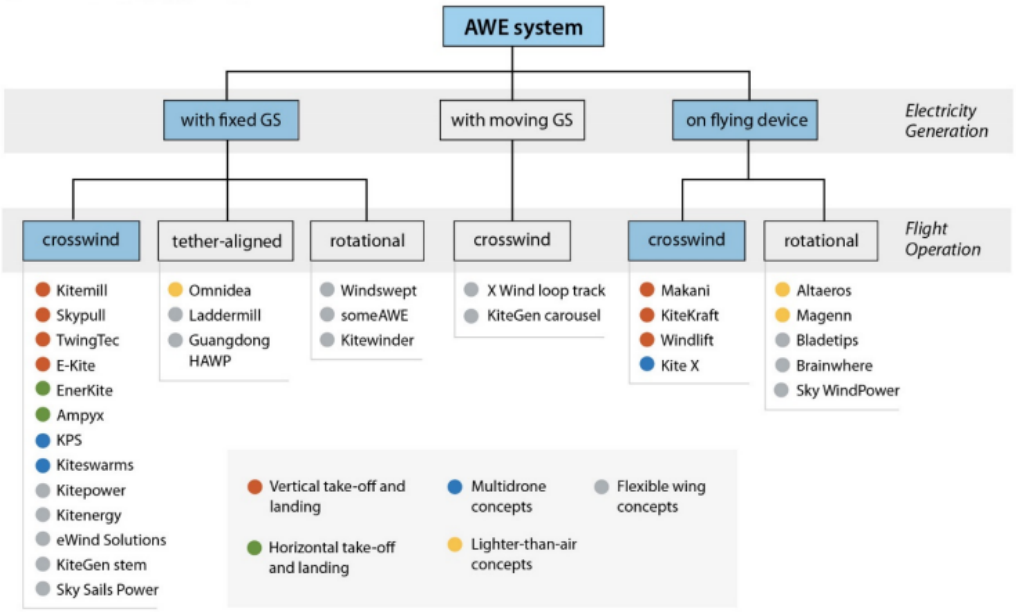

Figure 2.5: AWES Diversity Classification. (Source: [16])

Figure 2.6 illustrates a representative flight path for a Ground Generation AWES, showing the helical reel-out trajectory, the transition phase, and the reel-in maneuver back to the ground station, consistent with the pumping cycle described in Section 2.2 and the net positive energy balance of this cycle, where the energy harvested during reel-out significantly exceeds the energy consumed during reel-in. Here, the positive mechanical power generated (blue area) clearly outweighs the negative power consumed (red area) during a typical operation cycle, considering a constant ground wind velocity of 6 m/s.

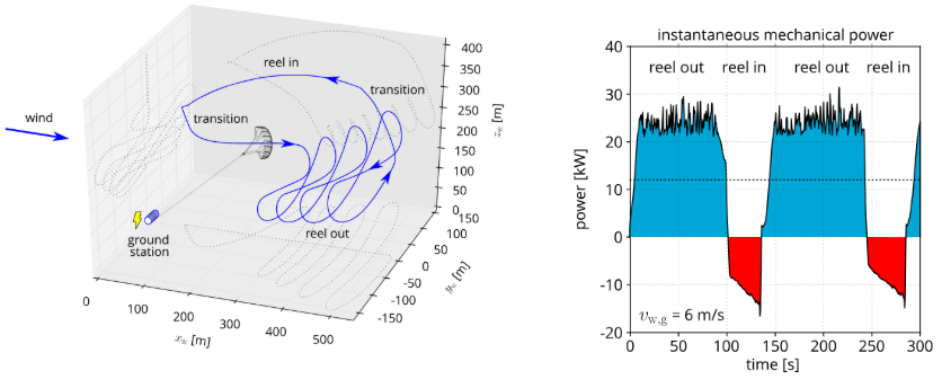

Figure 2.6: Kite Flight Path (Left) and Instantaneous Mechanical Power Output for a Ground-Generation AWES (Right). (Source: [8])

In addition to their operating principle, AWES can also be distinguished by the structural nature of the wing itself: soft, flexible wings, resembling surf kites or parachutes, and rigid wings, resembling small aircraft or the tips of conventional wind turbine blades [10]. As illustrated in Figure 2.7 (a), flexible wings rely solely on the aerodynamic load distribution generated by the airflow to maintain their shape, which allows them to be extremely lightweight relative to their surface area. This characteristic also makes them comparatively safer to operate, since a crash typically does not cause major structural damage, and their moderate flight speeds make them easier to control, even by a human pilot. Rigid wings, shown in Figure 2.7 (b), maintain their shape independently of the surrounding wind conditions, but require greater structural mass per unit of wing surface. Their higher lift-to-drag ratio allows them to reach significantly higher flight velocities, resulting in a higher power output per wing area, though this comes at the cost of greater potential damage in the event of a crash [10].

Many flexible wings already incorporate semi-rigid components, such as air-filled tubes (tube kites), to improve structural stability. One such hybrid concept, known as tensairity, employs pressurized air tubes combined with tension elements to increase the maximum wing loading while keeping the overall structure lightweight [10]. Figure 2.7 represents the resulting system layouts arising from these wing types: pumping power with a flexible wing (a), pumping power with a rigid wing (b), and onboard power generation (c).

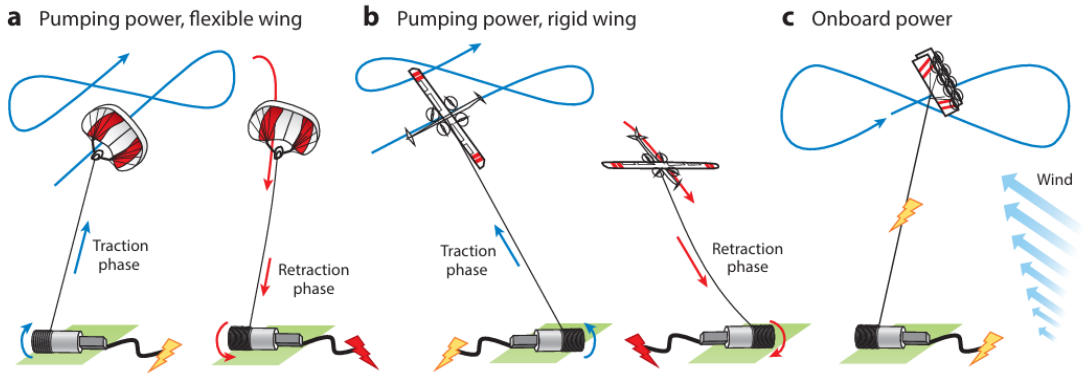

Figure 2.7: Different Types of Energy Conversion. (Source: [17])

2.4 Automatic Take-off and Landing

The transition of AWES into a commercially competitive renewable energy source is primarily contingent upon their ability to operate safely, reliably, and autonomously over extended periods and across diverse environmental conditions [18]. At present, most technological demonstrators have not reached full autonomy, as they continue to depend on human supervision during the critical Take-off and Landing phases.

Consequently, the development of robust ATOL schemes is a vital step toward operational maturity, as they must be specifically designed to handle the various types of wings and concepts [18].

The complexity of these maneuvers is heightened by the fact that TOL schemes differ significantly between AWES utilizing soft (flexible) wings and those using rigid wings. For both categories, a universally accepted or consensual specific scheme has yet to be established [19]. Within the scope of fixed-wing aircraft for ground-generation AWES, three primary self-propelled ATOL techniques are currently being studied. Several architectures can be distinguished such as Vertical Take-off and Landing, Horizontal Take-off and Landing or Circular Take-off and Landing, as shown in Figure 2.5. The following subsections examine each of these techniques in detail.

2.4.1 Vertical Take-off and Landing (VTOL)

This method operates similarly to standard multicopters, allowing the aircraft to ascend and descend vertically [19]. Industry developers have adopted VTOL schemes to overcome the need for expansive ground infrastructure and to enable fully autonomous operations. Pioneering projects like Makani Power [20], KiteMill [21] and TwingTec [22] applied this technique.

Makani developed a flying generator concept based on a rigid-wing glider with a double fuselage, placing it within the fixed-wing category. The aircraft was launched using onboard propellers, which were powered through a cable integrated into the tether whereas in calm wind conditions, these same propellers could also be used to maintain flight and avoid landing. Although the Makani concept was originally intended for both onshore and offshore deployment, further development was discontinued by Google for financial reasons, illustrating the considerable commercial and engineering challenges that remain in scaling AWES technology to a viable product [23]. Figure 2.8 demonstrates the prototype.

Figure 2.8: Makani Power VTOL Prototype. (Source: [24])

The VTOL strategies employed by KiteMill and TwingTec are fundamentally derived from conventional multicopter dynamics, utilizing integrated rotors with rotation axes perpendicular to the wing plane to facilitate vertical movement [4]. Despite this shared launch principle, the two

systems diverge significantly in how they manage rotor functionality during the transition to power production.

KiteMill has developed a Ground Generation concept based (Figure 2.9) on a rigid-wing glider, placing it within the rigid-kite category. The aircraft is launched vertically using onboard propellers powered by onboard batteries and once the kite reaches its operational altitude, starting with power production, the propellers fold away. In addition to enabling VTOL, these propellers can also serve as a redundancy mechanism in certain failure modes, since they remain capable of controlling the aircraft if needed. For its Ground Generation concept, KiteMill predominantly employs a circular flight path [23].

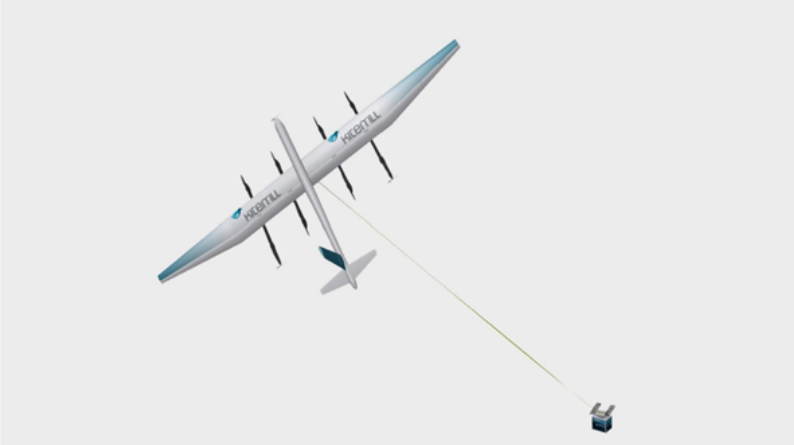

Figure 2.9: KiteMill VTOL Prototype. (Source: [4])

TwingTec has developed a pumping *yo-yo* concept (Figure 2.10) based on a highly efficient rigid wing connected to a single, non-conductive tether. The wing performs VTOL using rotors integrated into the airframe, which remain active only during the launch and landing phases and stay idle throughout power production. These rotors are powered by an onboard battery, which can in turn be recharged by a small onboard turbine, allowing fully automated launching and landing under a wide range of wind conditions. TwingTec also flies a helical flight path, and its systems, deployable in standard shipping containers up to 1 MW in capacity, are designed for both onshore and offshore use [23].

Figure 2.10: TwingTec VTOL Prototype. (Source: [9])

According to [19], VTOL requires the least amount of space for launch and recovery, as it simplifies the process of returning to the air after a temporary wind deficit. Nevertheless, high energy consumption is required during the hover phase to overcome gravity.

2.4.2 Horizontal Take-off and Landing (HTOL)

This approach involves a linear launch and landing process resembling a conventional airplane, though the tether remains fixed to the fuselage throughout the operation [19]. To minimize the spatial requirements of the launch platform, external power sources are utilized to achieve rapid acceleration of the flight unit. This reduction in footprint is typically accomplished through either catapult-assisted technology or by using the ground-based winch in motor mode to accelerate the aircraft via the tether [25].

Ampyx Power, now extinguished, has developed a pumping concept based on a glider with fixed wings and a double fuselage, placing it within the fixed-wing category. Landing follows a gliding approach, after which the aircraft is pulled back to its take-off position by the ground station via the tether. Like the TwingTec and Makani concepts, the Ampyx system was also designed for both onshore and offshore deployment [23]. The architecture features a catapult-assisted launch to reach flight velocity and a tether-based arresting system for recovery. This dual approach allows the system to operate from a significantly smaller ground station by mechanically managing the aircraft kinetic energy during the critical transition phases [9]. Figure 2.11 depicts the compact Ampyx Power architecture. To accommodate varying wind conditions, the platform is fully rotatable, ensuring that the system is always aligned with the wind direction.

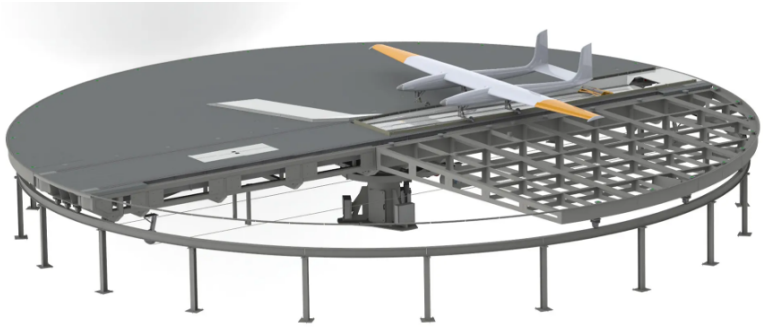

Figure 2.11: Ampyx Power HTOL Prototype. (Source: [25])

Additionally, ElektRail [26] is a company that introduced a TOL concept for Unmanned Aerial Vehicles (UAV). Figure 2.12 shows the mobile ground support that allows the deployment and retrieval of fixed-wing aircraft [27]. However, the landing maneuvers are of great complexity, which requires synchronization between the landing apparatus and the autonomous aircraft [9].

Figure 2.12: ElektRail HTOL Prototype. (Source: [27])

In accordance with [19], HTOL benefits from low power peak requirements, as it demands minimal additional mass for the climb phase. However, there is a significant limitation in the infrastructure, as the runway length must be sufficient for the aircraft to attain necessary take-off speeds for lift generation.

2.4.3 Circular Take-off and Landing (CTOL)

This technique utilizes circular motion for launch and recovery, with the tether secured to an anchorage point at the center of the rotation and attached to the wing of the aircraft [19]. Accordingly with [9, 4], the CTOL method operates on a straightforward principle of rotational acceleration. In this configuration, the kite gradually accumulates velocity through a series of expanding circular

maneuvers until it reaches the critical take-off speed and operational altitude necessary to initiate the power-production phase. Moreover, it is the least explored ATOL strategy.

Figure 2.13 illustrastes the model introduced by Antonello Cherubini, where an integrated motor system provides controlled thrust, driving the aircraft until it reaches the necessary take-off speed for an autonomous launch [9].

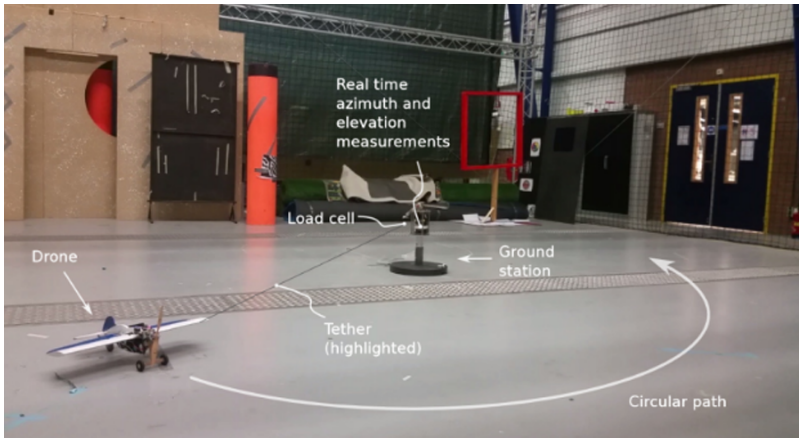

Figure 2.13: Experimental CTOL. (Source: [9])

EnerKite is one of the most experienced companies in the AWE field, as early as 2006, it was already preparing expert assessments and developing kite control systems, and from 2010 onward the company focused specifically on airborne wind converters based on semi-rigid wings and the pumping *yo-yo* concept [23]. The wing is steered passively from the ground station through three control ropes, an approach that enables operation across a wide range of wind conditions, fast and direct retraction during the reel-in phase and efficient power conversion. A rotating mast provides automatic launching and landing of the wing even in the absence of ground-level wind, with the wide operating range of this rotational launch extending the technology's applicability to low-wind regions. A proof of concept for this configuration was demonstrated at the end of 2021 and a subsequent full-cycle test flight conducted in 2022 demonstrated 17 consecutive operational cycles over 1.5 hours of flight, under wind speeds ranging from 1 to 8 m/s [23]. Regarding this technique, the aircraft fuselage is initially coupled to the terminal end of a motorized rotating mast. The rotational velocity induces the necessary aerodynamic lift and centrifugal loading, which collectively facilitate the passive reeling out of the tether [25]. To initiate landing, the helical flight path is mirrored through continuous tether retraction, bringing the kite into proximity with the ground station. The initial configuration of the EnerKite ground station, where the aircraft is mechanically secured to the distal end of a rotating arm, is illustrated in Figure 2.14.

Figure 2.14: EnerKite Rotational Arm. (Source: [4])

In CTOL the system generates an *infinite runway* [19], which facilitates the re-launching process. The system maintains low peak power requirements and avoids the additional mass penalties found in VTOL, as it does not require heavy on-board motors for climbing. A key drawback of this configuration, however, is the considerable ground area required, particularly for aircraft designs with large wingspans. Furthermore, as the least explored ATOL strategy, CTOL faces additional challenges in adapting existing aircraft and ground station technology, requiring further dedicated research to mature into a viable alternative.

2.5 UPWIND Project

As part of a global effort to harness high-altitude wind power, the University of Porto established the UPWIND project. The project serves as a multidisciplinary framework, combining theoretical research with practical experimental validation. While the focus of this project is the implementation of a TOL platform, the work directly supports the broader UPWIND research topics.

These operational goals are underpinned by identification, modeling, and estimation of AWES, which involve creating detailed models of kite generator systems and implementing state estimation methods like moving horizon estimation [5]. Furthermore, the work addresses the optimization and control of AWES by applying advanced techniques such as MPC to manage non-holonomic stability and utilizing adaptive mesh refinement to accelerate optimal control solvers for path following and power maximization. The research also extends to multiple kite systems, aiming to ensure overall system robustness through collision avoidance and determining the most effective layouts for kite arrays. This project contributes to several foundational research topics within the UPWIND initiative, starting with the development of ATOL procedures through the exploration of CTOL.

The UPWIND project employs a small-scale fixed-wing aircraft integrated into a ground-based power generation system. Figure 2.15 depicts a fixed wing aircraft used in the project, built from lightweight extended foam and is dimensioned to support a power extraction capacity of 1.5 to

5 kW. The aircraft configuration includes landing gear and an onboard propulsion system, allowing CTOL configuration. During the power generation phase it becomes desirable to minimize airborne mass in order to maximize aerodynamic and energetic performance. For this reason, relying solely on onboard propulsion for ATOL becomes less attractive. This setup operates as the foundational physical model to validate the implemented algorithms. To assist the TOL of the aircraft, the ground station also features an auxiliary vehicle, from now on designated as cart, which dynamically rotates synchronized with the circular flight path of the kite. The physical hardware implementation of this platform is further detailed in Section 5.2.2.

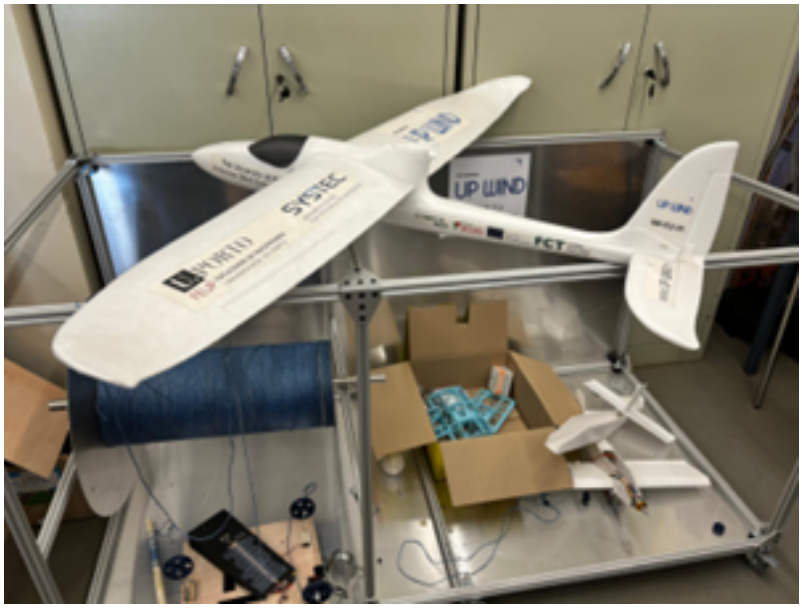

Figure 2.15: UPWIND Aircraft Prototype. (Source: [9])

Chapter 3

Kite-Cart System Dynamics

This chapter establishes the kinematic and dynamic modeling frameworks for the kite-cart system. It covers the essential coordinate transformations, rotation matrices, and aerodynamic principles governing the small-scale aircraft (Section 2.5), followed by the state-space formulation and physical constraints of the tracking cart. Finally, the spatial coupling between both vehicles is formalized, providing the dynamical foundation required for the synchronization algorithms developed in Chapter 4.

3.1 Coordinate Frames

When studying the motion of the kite, it is crucial to understand the orientation of distinct bodies, relative to each other. So, it is important to comprehend how the aircraft is oriented with respect of the earth.

- **Global Frame**: This is the global coordinate system, represented by the basis $(\vec{e}_x, \vec{e}_y, \vec{e}_z)$.
- **Local Frame**: This is the local coordinate system, mainly represented by spherical coordinates (r, φ, β). The length of the tether is given by r, the azimuthal angle is symbolized by φ and the elevation angle typified as β, whose basis is $(\vec{e}_r, \vec{e}_\varphi, \vec{e}_\beta)$.
- **Body Frame**: The kite orientation is described by an intrinsic coordinate system $(\vec{e}_X, \vec{e}_Y, \vec{e}_Z)$. The basis vectors are $\vec{e}_X$ (Roll) which coincides with the forward-pointing longitudinal axis, $\vec{e}_Y$ (Pitch) aligns with the transversal axis pointing towards the right wing and $\vec{e}_Z$ (Yaw) points vertically downward from the aircraft belly. Figure 3.1 schematizes this coordinate system.

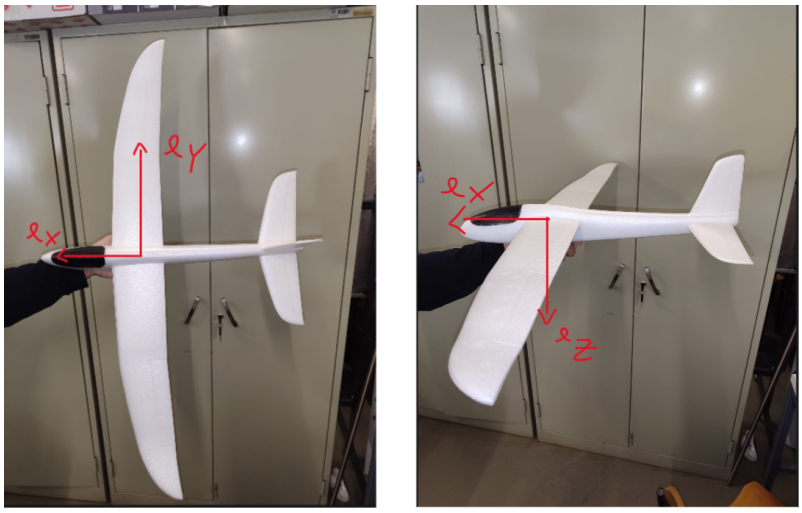

Figure 3.1: Body Frame (Coordinate System): Top and Side Views.

- **Tangent Plane** τ: A local tangent plane, defined by the orthonormal basis $(\vec{e}_r, \vec{e}_\varphi, \vec{e}_\beta)$, follows the kite position on a spherical manifold. The radius of the sphere r corresponds to the instantaneous tether length with the ground station serving as the center of the coordinate system. Figure 3.2 illustrates the operational envelope of the kite, depicting the tangent plane τ.

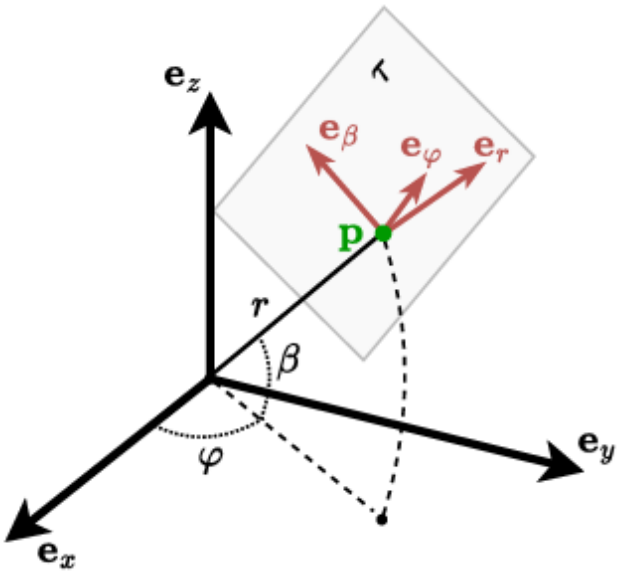

Figure 3.2: Global and Local Frames and Tangent Plane τ at Position p. (Source: Adapted from [4])

3.2 Rotation Matrices

To characterize the relative pose of one rigid body with respect to another, fixed coordinate frames are assigned to each body, enabling the mathematical definition of their spatial geometric relationships. By establishing these reference frames, the system can precisely map the displacement and rotation required to transition between the bodies respective positions. As Figure 3.3 illustrates, the vector p can be expressed in both frame F^0 and F^1. F^0 is specified by (i^0, j^0, k^0), whereas F^1 is given by (i^1, j^1, k^1) [28].

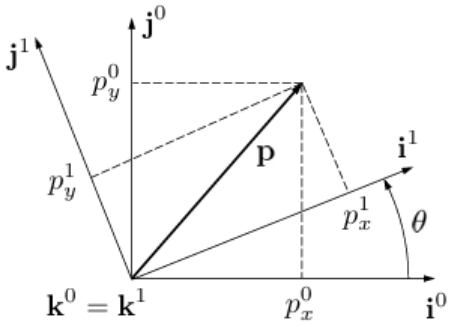

Figure 3.3: 2D Rotation Frames. (Source: [28])

When representing p in the frame F^0, it is formulated as

$$p^0 = p_x^0 i^0 + p_y^0 j^0 + p_z^0 k^0. \tag{3.1}$$

The same happens when formulating it in the frame F^1, as p is expressed as

$$p^1 = p_x^1 i^1 + p_y^1 j^1 + p_z^1 k^1. \tag{3.2}$$

Expressing Equation 3.1 and Equation 3.2 in matrix form, the result is given by

$$R_0^1 = \begin{bmatrix} i^1 \cdot i^0 & i^1 \cdot j^0 & i^1 \cdot k^0 \\ j^1 \cdot i^0 & j^1 \cdot j^0 & j^1 \cdot k^0 \\ k^1 \cdot i^0 & k^1 \cdot j^0 & k^1 \cdot k^0 \end{bmatrix}. \tag{3.3}$$

Taking Figure 3.3 into account, it is possible to relate Equations 3.1, 3.2 and 3.3, leading to

$$p^1 = R_0^1 p^0. \tag{3.4}$$

Each coordinate frame, stated in Section 3.1, allows an improved approach to certain models, so that rotation matrices are used to convert these coordinate systems.

Starting by converting from Local to Global Frame

$$R_L^G = \begin{bmatrix} cos(\beta)cos(\varphi) & -sin(\varphi) & -sin(\beta)cos(\varphi) \\ cos(\beta)sin(\varphi) & cos(\varphi) & -sin(\beta)sin(\varphi) \\ sin(\beta) & 0 & cos(\beta) \end{bmatrix}. \tag{3.5}$$

Applying one of the properties of the rotation matrices it is possible to convert from Global to Local Frame is

$$R_0^1 = (R_1^0)^T = (R_1^0)^{-1}, \tag{3.6}$$

obtaining

$$R_G^L = (R_L^G)^T = \begin{bmatrix} \cos(\beta)\cos(\varphi) & \cos(\beta)\sin(\varphi) & \sin(\beta) \\ -\sin(\varphi) & \cos(\varphi) & 0 \\ -\sin(\beta)\cos(\varphi) & -\sin(\beta)\sin(\varphi) & \cos(\beta) \end{bmatrix}. \tag{3.7}$$

3.3 Tethered Aircraft Kinematics

The kinematics of a tethered aircraft are most effectively described using a spherical coordinate system (r, φ, β) originating at the ground anchorage point.

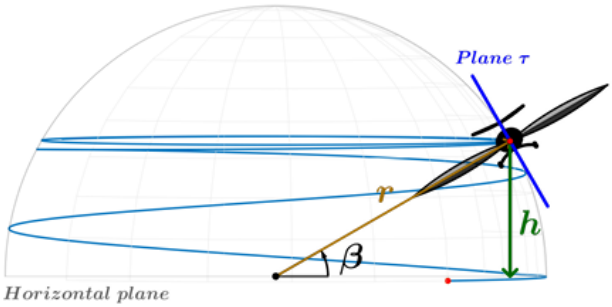

Figure 3.4: Circular Take-off Trajectory. (Source: [18])

Regarding Figure 3.4, a plane τ is tangential to the spherical surface of the flight envelope and lies perpendicular to the radial tether vector. The position, velocity and acceleration vectors are respectively defined as

$$p = \begin{bmatrix} r \\ \varphi \\ \beta \end{bmatrix}_{\mathrm{L}}, \tag{3.8}$$

$$\dot{p} = \begin{bmatrix} \dot{r} \\ r\cos\beta\,\dot{\varphi} \\ r\dot{\beta} \end{bmatrix}_{\mathrm{L}}, \tag{3.9}$$

$$\ddot{p} = \begin{bmatrix} \ddot{r} \\ r\cos\beta\,\ddot{\varphi} \\ r\ddot{\beta} \end{bmatrix}_{\mathrm{L}} + \begin{bmatrix} -r\dot{\beta}^2 - r\dot{\varphi}^2\cos^2\beta \\ 2\dot{r}\dot{\varphi}\cos\beta - 2r\dot{\varphi}\dot{\beta}\sin\beta \\ 2\dot{r}\dot{\beta} + r\dot{\varphi}^2\cos\beta\sin\beta \end{bmatrix}_{\mathrm{L}}. \tag{3.10}$$

A body-fixed reference frame is established at the aircraft center of mass, defined by the orthonormal basis $(\vec{e}_X, \vec{e}_Y, \vec{e}_Z)$. In this convention, the longitudinal axis $\vec{e}_X$ is directed toward the nose, the lateral axis $\vec{e}_Y$ extends through the right wing, and the normal axis $\vec{e}_Z$ points downward through the fuselage, consistent with standard aircraft body-frame conventions seen before.

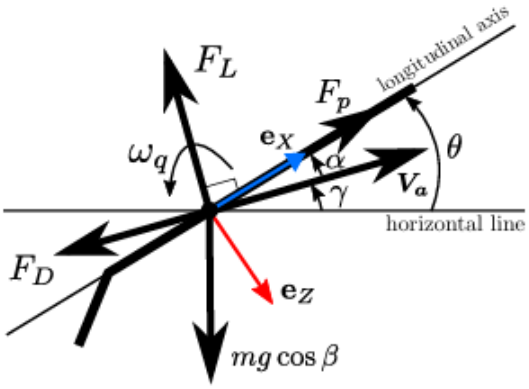

Figure 3.5: Aircraft Longitudinal Model. (Source: [18])

According to Figure 3.5, θ represents the pitch angle, which corresponds to the angle defined by the horizontal line and $\vec{e}_X$, the longitudinal axis. The airspeed V_a along the horizontal line defines the flight-path angle γ and the aircraft's inertial velocity is denoted by V, such that

$$V_{\mathrm{a}} = V - V_{\mathrm{w}}, \tag{3.11}$$

where V_{w} denotes the wind velocity, considered zero throughout this work, which leads to $V_{\mathrm{a}} = V$.

On the other hand, the angle of attack α is the angle between V_a and $\vec{e}_X$. The relation between γ and θ is given by

$$\theta = \gamma + \alpha, \tag{3.12}$$

The aircraft complies with the following kinematics equations

$$\begin{aligned} r\cos\beta\,\dot{\varphi} &= V_a\cos\gamma \\ r\dot{\beta} &= V_a\sin\gamma \\ \dot{\theta} &= \omega_q, \end{aligned} \tag{3.13}$$

where ω_q stands for the pitch rate.

Proceeding to the derivative of the kinematics (Equation 3.13), it yields to

$$\begin{aligned} r\ddot{\beta} &= \dot{V}_a \sin\gamma + V_a \cos\gamma\dot{\gamma} \\ r\cos\beta\ddot{\varphi} &= \dot{V}_a \cos\gamma - V_a\dot{\gamma}\sin\gamma + \frac{V_a^2}{r}\tan\beta\cos\gamma\sin\gamma \end{aligned} . \tag{3.14}$$

3.4 Actuating Forces

There is a set of forces that act on the kite, which characterizes the behavior of the system in both local and body fixed frames, such as aerodynamic lift ($\vec{F}^{\text{Lift}}$) and aerodynamic drag ($\vec{F}^{\text{Drag}}$) , tether tension ($\vec{F}^{\text{Tether}}$), thrust ($\vec{F}^{\text{Thrust}}$) and gravity ($\vec{F}^{\text{Gravity}}$) which are resolved using the coordinate transformations established in the previous section ([29], [18]).

When adopting a non-inertial reference frame, the governing equations must be augmented with inertial forces to account for the frames rotation, specifically, the centrifugal ($\vec{F}^{\text{Centrifugal}}$) and Coriolis ($\vec{F}^{\text{Coriolis}}$) terms are introduced.

The dynamic behavior of the kite is determined by the total resultant force acting on the system. In the non-inertial frame, the total force ($\vec{F}^{\text{Total}}$) can be expressed as

$$\vec{F}^{\text{Total}} = \begin{bmatrix} \vec{F}_r \\ \vec{F}_\varphi \\ \vec{F}_\beta \end{bmatrix} = \vec{F}^{\text{Lift}} + \vec{F}^{\text{Drag}} + \vec{F}^{\text{Tether}} + \vec{F}^{\text{Thrust}} + \vec{F}^{\text{Gravity}} + \vec{F}^{\text{Centrifugal}} + \vec{F}^{\text{Coriolis}}. \tag{3.15}$$

Relating Equations 3.10 and 3.15, taking into consideration the mass m of the kite, Newton´s Second Law is applied, such that

$$m\ddot{p} = \vec{F}^{\text{Total}}. \tag{3.16}$$

$\vec{F}^{\text{Lift}}$ and $\vec{F}^{\text{Drag}}$ are expressed as

$$\vec{F}^{\text{Lift}} = F_{\text{L}}\vec{e_{Lift}} = \frac{1}{2}\rho A\|V_a\|^2 c_L(\alpha), \tag{3.17}$$

$$\vec{F}^{\text{Drag}} = F_{\text{D}}\vec{e_{Drag}} = -\frac{1}{2}\rho A\|V_a\|^2 c_D(\alpha), \tag{3.18}$$

where $c_L(\alpha)$ and $c_D(\alpha)$ represent the lift and drag coefficients, respectively.

The remaining force components acting on the system in the respective coordinate frames are defined as follows

$$\vec{F}^{\text{Tether}} = -T\,\vec{e}_r = \begin{bmatrix} -T \\ 0 \\ 0 \end{bmatrix}_{\text{L}}, \tag{3.19}$$

where T stands for the tension of the tether.

$$\vec{F}^{\text{Thrust}} = F_P \vec{e_X} = \begin{bmatrix} F_P \\ 0 \\ 0 \end{bmatrix}_{\text{B}}, \tag{3.20}$$

where F_P represents the controlled thrust magnitude.

Then, the gravity is expressed as

$$\vec{F}^{\text{Gravity}} = mg\,\vec{e}_z = \begin{bmatrix} 0 \\ 0 \\ mg \end{bmatrix}_{\text{G}}. \tag{3.21}$$

Applying the rotation matrix property expressed in Equation 3.7, the gravity force in the global frame can be converted to the local coordinate frame, then Equation 3.21 becomes

$$\vec{F}^{\text{Gravity}} = R_G^L \begin{bmatrix} 0 \\ 0 \\ mg \end{bmatrix}_G = \begin{bmatrix} mg\sin\beta \\ 0 \\ mg\cos\beta \end{bmatrix}_L. \tag{3.22}$$

Taking into account the acceleration vector $\ddot{p}$ (Equation 3.10), the second term represents the contribution of the inertial forces, $\vec{F}^{\text{Centrifugal}}$ and $\vec{F}^{\text{Coriolis}}$

$$\ddot{p} = \begin{bmatrix} \ddot{r} \\ r\cos\beta\,\ddot{\varphi} \\ r\ddot{\beta} \end{bmatrix}_{\text{L}} + \underbrace{\begin{bmatrix} -r\dot{\beta}^2 - r\dot{\varphi}^2\cos^2(\beta) \\ 2\dot{r}\dot{\varphi}\cos(\beta) - 2r\dot{\varphi}\dot{\beta}\sin(\beta) \\ 2\dot{r}\dot{\beta} + r\dot{\varphi}^2\cos(\beta)\sin(\beta) \end{bmatrix}_L}_{-1/m\vec{F}^{\text{inert}}}. \tag{3.23}$$

Combining Equation 3.16 with Equation 3.23, a new dynamic expression is established

$$m \begin{bmatrix} \ddot{r} \\ r\ddot{\varphi}\cos(\beta) \\ r\ddot{\beta} \end{bmatrix}_L = \vec{F}^{\text{Lift}} + \vec{F}^{\text{Drag}} + \vec{F}^{\text{Tether}} + \vec{F}^{\text{Thrust}} + \vec{F}^{\text{Gravity}} + \vec{F}^{\text{Inertia}}, \tag{3.24}$$

from which $\dot{V}_a$ and $\dot{\gamma}$ can be obtained. For more information, see [18].

3.5 Kite Model

To fully characterize the kite behavior, the system is cast into a state-space representation. This framework consolidates the kinematic variables (Section 3.3), namely the kite´s position and velocity expressed in the spherical basis (r,φ,β), with the dynamic influences acting upon the airframe (Section 3.4).

The state-space model is given by

$$\dot{X}_{\text{kite}} = f(X_{\text{kite}}, u_{\text{kite}}) \iff \tag{3.25}$$

$$\iff \begin{bmatrix} \dot{\varphi} \\ \dot{\beta} \\ \dot{V}_a \\ \dot{\gamma} \\ \dot{\theta} \end{bmatrix} = \begin{bmatrix} \frac{1}{r\cos(\beta)} V_a \cos\gamma \\ \frac{1}{r} V_a \sin\gamma \\ \frac{1}{m}\left(-F_D + F_P\cos\alpha - mg\cos\beta\sin\gamma\right) \\ F_P\sin\alpha - mg\cos\beta\cos\gamma - \frac{mV_a^2}{r}\tan\beta\cos\gamma \\ \omega_q \end{bmatrix} \tag{3.26}$$

$$X_{kite} = \begin{bmatrix} \varphi \\ \beta \\ V_a \\ \gamma \\ \theta \end{bmatrix} \qquad and \qquad u_{kite} = \begin{bmatrix} F_P \\ \omega_q \end{bmatrix}. \tag{3.27}$$

3.6 Cart Model

Complementing the kite dynamics introduced in Section 3.5, the ground-based cart is modeled as a point mass constrained to move along the circular track whose radius R corresponds to the horizontal projection of the tether length. Since the cart's motion is restricted to this single degree of freedom, its dynamics can be fully captured by a reduced state-space representation, considerably simpler than that of the kite. The state-space model is given by

$$\dot{X}_{\text{cart}} = f(X_{\text{cart}}, u_{\text{cart}}) \iff \tag{3.28}$$

$$\iff \begin{bmatrix} \dot{\varphi}_c \\ \dot{\omega}_c \end{bmatrix} = \begin{bmatrix} \omega_c \\ \frac{a_c}{R} \end{bmatrix} \tag{3.29}$$

$$X_{\text{cart}} = \begin{bmatrix} \varphi_c \\ \omega_c \end{bmatrix} \qquad and \qquad u_{\text{cart}} = a_c. \tag{3.30}$$

The state vector of the cart X_{cart} is defined by its angular position φ_c and its angular velocity ω_c. The input vector u_{cart} stands for the linear acceleration command a_c which, divided by the track radius R, yields the carts angular acceleration $\dot{\omega}_c$, as reflected in Equation 3.29.

To ensure that the control yields realizable trajectories, the cart model must respect several physical limitations imposed by the structural integrity of the track and the capabilities of the

actuation system. Accordingly, the control input and the state variables are subject to saturation constraints

$$\begin{aligned} |a_c| &\leq a_{c,\max} \\ 0 \leq \omega_c &\leq \omega_{c,\max} \end{aligned}, \tag{3.31}$$

where the linear acceleration $a_{c,\max}$ represents the maximum acceleration and braking capacities of the cart. Regarding the angular velocity, the lower bound enforces a strict unidirectional movement ($\omega_c \geq 0$), preventing the cart from reversing along the circular path during the synchronization phase, a behavior that would be physically inconsistent with the forward-only tracking strategy adopted throughout this work. Exceeding the upper bound $\omega_{c,\max}$ could induce excessive tension on the tether, potentially compromising the flight stability or the structural integrity of the kite-cart system coupling. The primary objective of the coordinated control framework is to guarantee that the ground platform tracks the aircraft's azimuthal motion as closely as possible throughout all mission phases. To this end, the spatial synchronization between the two vehicles is parameterized through the azimuthal phase error $\Delta\varphi$ defined as

$$\Delta\varphi = \varphi - \varphi_c, \tag{3.32}$$

where φ denotes the azimuthal position of the aircraft, as defined in the kite state vector of Equation 3.27. A forward error formulation is implemented to guarantee optimal convergence characteristics under large initial misalignments and to eliminate numerical discontinuities within the control loops. This metric acts as the primary feedback variable for the synchronization algorithms developed in Chapter 4, enabling the tracking laws to dynamically modulate the cart's acceleration command a_c in response to the relative position and velocity of the aircraft.

Chapter 4

Synchronization of Kite-Cart System for Circular Landing

This chapter introduces the analysis of CTOL using the UPWIND aircraft and ground cart prototype (Section 2.5). The main contribution consists on a novel synchronization and capture control framework. Aligning the kite dynamics with the cart dynamics, described in Chapter 3, moving in a circular platform, the proposed strategy ensures reliable autonomous landing.

4.1 Control Architecture

The control framework is structured into a three-tier hierarchical architecture, specifically engineered to manage the complexities of autonomous landing. The Supervisory Layer occupies the highest level, governing mission phase transitions and generating reference trajectories. Subordinate to this, the Kite Control Layer maintains the aircraft flight envelope, regulating airspeed, attitude, and altitude via an integrated PID and LQR approach. The architecture is completed by the Cart Control Layer, which utilizes angular velocity feedback to achieve precise synchronization between the ground platform and the aircraft.

The autonomous mission is orchestrated through a finite state machine composed of eight sequential phases, as depicted in Figure 4.1. The operation begins with Ground Acceleration (P1), where the aircraft increases its airspeed until reaching the rotation threshold (V_{rot}), followed by the Rotation maneuver (P2) to establish the required pitch angle. Upon departure from the ground, the system enters the Initial Climb (P3) to gain altitude at a stabilized airspeed, subsequently transitioning into a steady Horizontal Loiter (P4). The landing sequence commences with a Deceleration phase (P5) to reach glide velocity, leading into a stabilized Descent (P6) at a constant glide angle. The final approach is governed by the Flare maneuver (P7) to minimize vertical impact, concluding with the Rest phase (P8) for post-landing deceleration and complete stop.

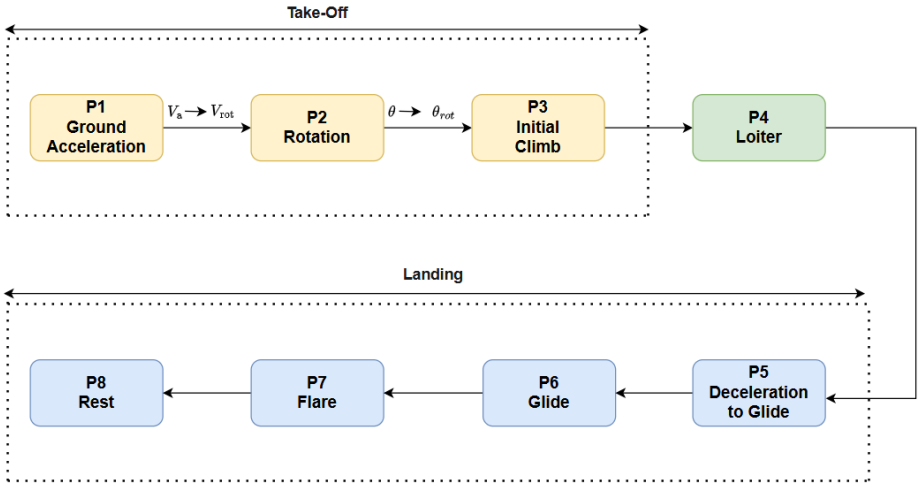

Figure 4.1: State Machine Describing the Flight Phases: Take-Off (Light Yellow), Loiter (Light Green) and Landing (Light Blue). (Source: [18])

4.2 Kite Control Laws

The kite flight control system is synthesized through a hybrid architecture that alternates between PID and Linear Quadratic Regulator (LQR) controllers, specifically tailored to the operational requirements of each flight phase. For regimes characterized by single-variable regulation, such as phases P1, P2, P5, and P7, PID controllers are employed. Starting by P1, a velocity-based PID regulates the airspeed V_a via thrust commands, whereas during P2 and P7, the control logic focuses on attitude regulation. In these stages, a pitch-tracking PID is used to follow the reference angle θ_{ref}, with the particularity that the flare maneuver is executed under zero-thrust conditions to facilitate a smooth touchdown. For the more complex phases requiring multi variable regulation, namely P3, P4, and P6, a local LQR framework is designed to manage the coupled longitudinal dynamics. The synthesis of these controllers follows a systematic three-step procedure. First, a steady-state reference x_{ref} is established to be consistent with the specific phase objectives. Subsequently, the aircraft's non-linear dynamics are linearized around this operating point to derive a state-space representation. Finally, an optimal feedback gain is calculated by minimizing the quadratic cost function

$$J = \int_0^\infty (x_e^T Q x_e + u_e^T R u_e)\, dt, \tag{4.1}$$

where x_e and u_e represent the deviations from the state and control references, respectively. The weighting matrices Q and R are chosen as diagonal and are specifically tuned for each flight regime to balance tracking performance with actuator effort. For more information about the Kite control, see [18].

4.3 Cart Control Law

The control strategy for the ground platform is synthesized to ensure azimuthal synchronization with the aircraft, being divided into two operational regimes: the Tracking Phase and the Landing Phase. In the first regime, which encompasses phases P1 through P5, the primary objective is to minimize the azimuthal phase error between the two vehicles. To achieve this, a multi-component linear acceleration command a_c is formulated as

$$a_c = R\left(K_p \tanh(\Delta\varphi) + K_f(\dot{\varphi} - \omega_c) - K_d\omega_c + a_{c,i} + a_{c,i_{vel}}\right), \tag{4.2}$$

where K_p represents a non-linear proportional gain utilizing a hyperbolic tangent function (tanh) for soft saturation, K_f is a feedforward gain designed to match the cart velocity ω_c to the aircraft azimuthal angular velocity $\dot{\varphi}$ and K_d serves as a derivative gain for system damping. The terms $a_{c,i}$ (Equation 4.3) and $a_{c,i_{vel}}$ (Equation 4.4) introduce integral action on, respectively, the phase error and the angular velocity error

$$a_{c,i}(t) = \text{sat}_{[-1,8]}\left(K_i \int_0^t \Delta\varphi \, d\tau\right), \tag{4.3}$$

$$a_{c,i_{vel}}(t) = \text{sat}_{[0,5]}\left(K_{i_{vel}} \int_0^t (\dot{\varphi} - \omega_c) \, d\tau\right), \tag{4.4}$$

where $\text{sat}_{[\cdot,\cdot]}$ denotes saturation within the indicated bounds, independently applied to each integrator to prevent unbounded accumulation. These integral terms were introduced during controller tuning to eliminate the residual steady-state velocity and phase offsets observed when relying on the proportional, feedforward, and derivative action of the original formulation, particularly following transient maneuvers such as the cart's initial acceleration toward the azimuthal position of the kite. The complete set of gains, K_f, K_p, K_d, K_i, $K_{i_{vel}}$, and parameters is summarized in Table 4.1.

Table 4.1: Simulation Parameters and Controller Gains.

Parameter	**Symbol**	**Value**
Wing area	A	1.225 m^2
Mass	m	1.0 kg
Tether length	R	18.0 m
Target altitude	h_{land}	0.15 m
Proportional gain	K_p	70
Feedforward gain	K_f	50
Derivative gain	K_d	2
Integral	K_i	0
	$K_{i_{vel}}$	0

The kite angular velocity is simply calculated as

$$\dot{\varphi} = \frac{V_a \cos(\gamma)}{R\cos(\beta)}, \tag{4.5}$$

where R denotes the radius of the circular ground track followed by the cart, directly corresponding to the horizontal projection of the tether length. To ensure physically consistent behavior, the controller explicitly enforces actuator saturation and rate limits, such as constraining the angular velocity to be non-negative to prevent reverse motion. Furthermore, a forward-only angular error formulation is adopted to avoid discontinuities in the synchronization variable, thereby improving convergence properties during large phase offsets. As the mission transitions to the Landing Phase (P5-P8), the control objective shifts to support the aerodynamic requirements of the kite. During this approach, the cart must maintain a minimum linear velocity v_{min} to ensure sufficient lift for the kite. The reference angular velocity $\omega_{c,ref}$ which prevents underspeed conditions that could compromise lift support, ensuring the existence of a feasible capture trajectory until the system reaches a complete stop is given by

$$\omega_{c,ref} = \max\left(\dot{\varphi}, \frac{v_{min}}{R}\right). \tag{4.6}$$

4.4 Autonomous Capture Strategy

The successful conclusion of the autonomous mission requires a well-defined criterion for transitioning from active flight control to the final capture and rest phase (P8). Rather than relying on a single threshold, the structural capture of the system is modeled as a hybrid event, dynamically triggered at the exact instant when three independent state conditions are simultaneously satisfied

$$|\Delta\varphi| \leq \Delta\varphi_{\max}, \tag{4.7}$$

$$h \leq h_{\text{land}}, \tag{4.8}$$

$$V_{\min} \leq V \leq V_{\max}. \tag{4.9}$$

where Equations 4.7, 4.8 and 4.9 stands for the angular alignment, altitude condition and speed window conditions, respectively. Equation 4.7 bounds the azimuthal synchronization error between the kite and the cart within an acceptable tolerance $\Delta\varphi_{\max}$, Equation 4.8 requires the aircraft altitude h to have descended below the landing threshold h_{land} and Equation 4.9 restricts the kite's airspeed V to a window bounded by a minimum value V_{min}, below which lift cannot be sustained and a maximum value V_{max}, above which the capture would impose excessive mechanical loads on the cart's coupling mechanism.

The capture sequence is initiated once all three window conditions remain concurrently satisfied for a minimum duration, usually 2 to 3 seconds. Upon successful capture, the cart azimuth is synchronized and locked to the aircraft azimuth ($\varphi = \varphi_c$), the aircraft matches its velocity ($V = v_c$),

and the system transitions the aircraft to a rest state (P8) utilizing momentum transfer control. Conversely, if these capture criteria are not fulfilled before the altitude drops below a critical threshold ($h < h_{\text{land}}$), the system aborts the cart capture and triggers an immediate ground touchdown.

4.5 Simulation Results

To assess the performance of the proposed synchronization architecture, a comprehensive numerical simulation scenario was developed to encompass all operational mission phases, described in Figure 4.1. The simulation framework was implemented in MATLAB, utilizing a fixed time step of $\Delta t = 0.02$s over a total time window T of 80 s. The sequential progression of the autonomous mission, showcasing the interaction between the kite and the ground ground cart is illustrated through the 3D trajectories, presented in Figure 4.2 and Figure 4.3. Figure 4.2 details the initial operational stages, encompassing phases P1 through P4, while Figure 4.3 presents the subsequent execution from phase P5 to the last phase P8.

In each subplot, the green horizontal plane represents the circular ground track where the autonomous cart operates. The blue spatial curve delineates the continuous 3D flight trajectory computed for the kite and the straight line connecting the two agents symbolizes the physical tether, highlighting the variable geometric constraints throughout the maneuver. As observed in Figure 4.2, the sequence initiates with the system preparing the initial acceleration and deployment, followed by the gradual tensioning and ascension phases where the kite transitions into its periodic crosswind-like circular loitering envelope. Moving to Figure 4.3, phases P5 to P8 demonstrate the synchronization capabilities of the proposed control laws. Even as the kite scales its altitude or modulates its pitch and propeller forces, the ground cart dynamically adjusts its azimuthal position along the circular track, consistently aligning itself with the airborne agent to minimize the angular tracking error and guarantee a controlled, automated landing approach.

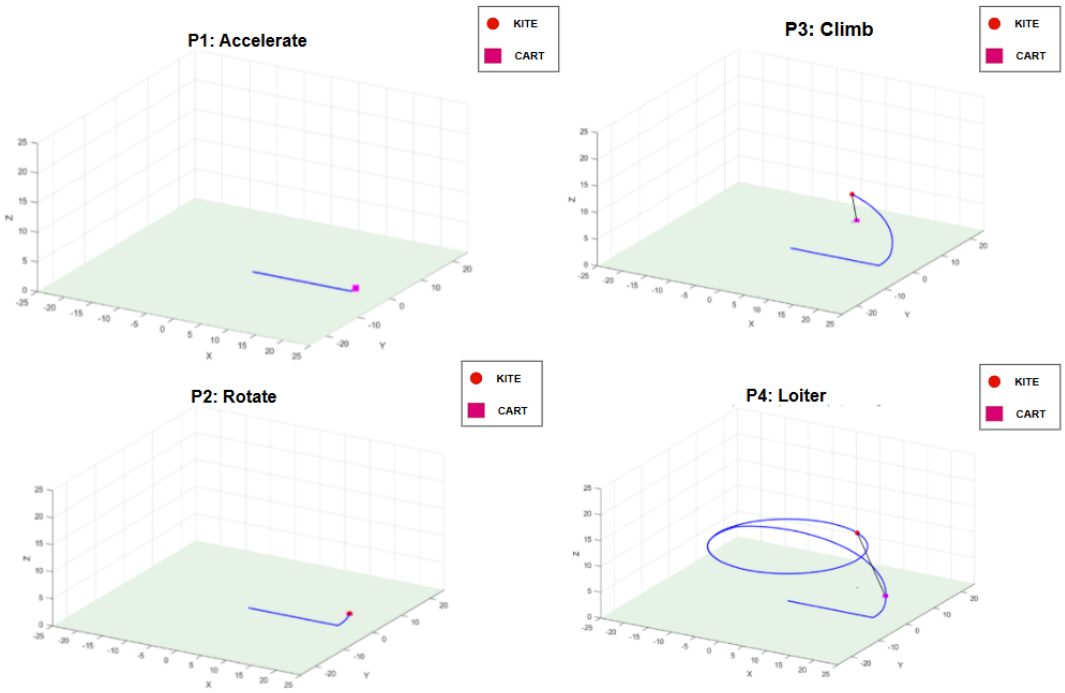

Figure 4.2: Flight Phases in MATLAB (P1-P4).

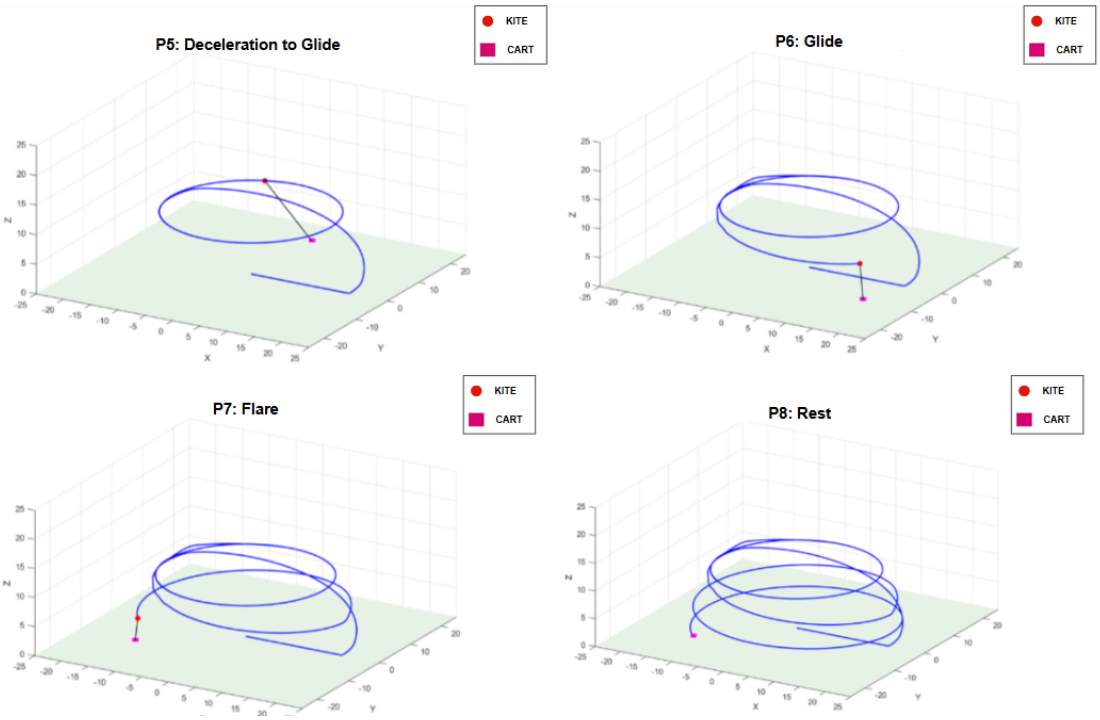

Figure 4.3: Flight Phases in MATLAB (P5-P8).

Analyzing Figures 4.4 and 4.5, several critical insights can be deduced from the synchronization performance analysis. Throughout phases P1 to P5, the synchronization error is tightly bounded, a response primarily attributed to the effective integration of the feedforward control action. As the mission transitions into phases P6 and P7, the system exhibits further narrowed error bounds, ensuring a robust stabilization profile in preparation for the physical capture. Crucially, the residual synchronization error at the exact instance of capture satisfies the strict geometric tolerances dictated by the predefined capture window requirements.

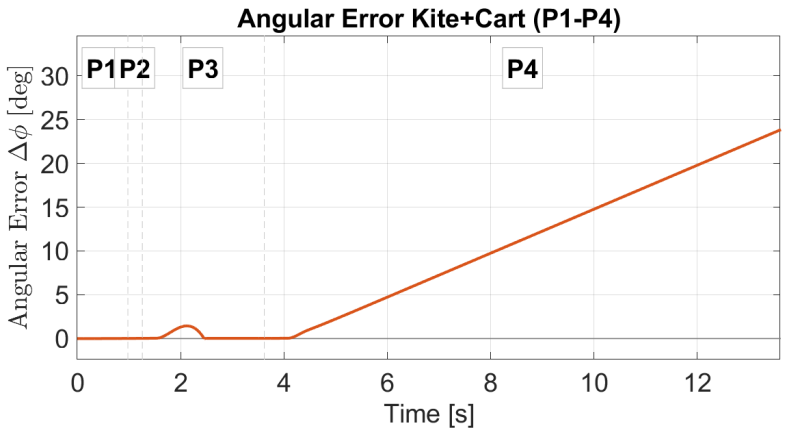

Figure 4.4: Angular Error of the Kite-Cart System (P1-P4).

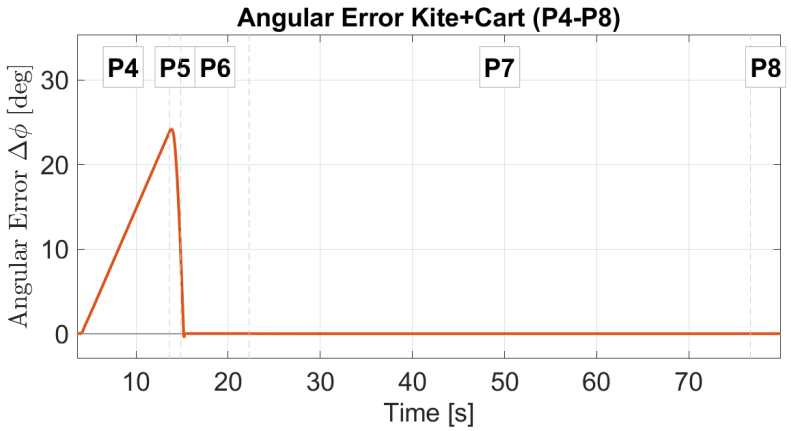

Figure 4.5: Angular Error of the Kite-Cart System (P4-P8).

Based on Figures 4.6 and 4.7, some critical observations can be deduced regarding the velocity synchronization between the two vehicles. First, the ground cart velocity exhibits high-fidelity tracking of the aircraft velocity profile throughout the entire mission with minimal transient delay, demonstrating the high authority of the distributed coordination logic. During phase P7, the aircraft undergoes a planned, controlled deceleration, while the tracking cart adaptively modulates its velocity to match the predefined landing profile. Ultimately, at the precise instance of touchdown, the minimized velocity differential ensures a low-impact, soft capture sequence.

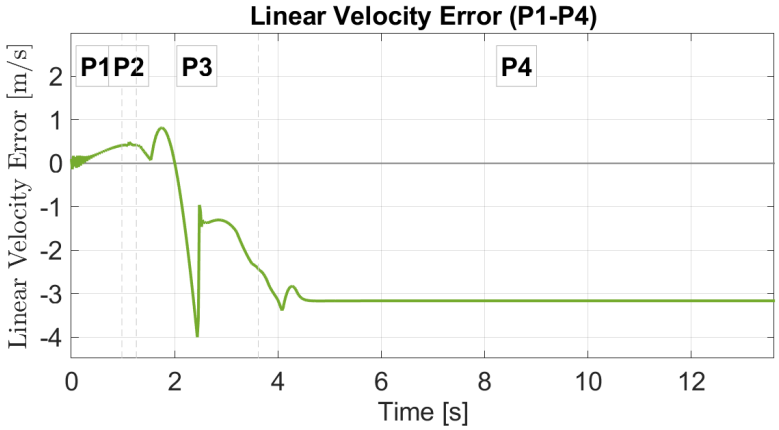

Figure 4.6: Linear Velocity Error of the Kite-Cart System (P1-P4).

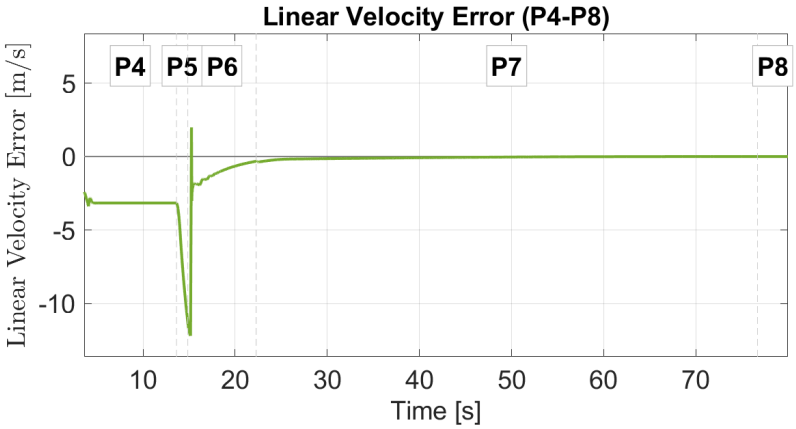

Figure 4.7: Linear Velocity Error of the Kite-Cart System (P4-P8).

Regarding Figures 4.8 and 4.9, during phases P1 and P2, the control system commands maximum thrust alongside an aggressive pitch rate to facilitate a rapid take-off rotation and lift-off sequence. Phase P4 is characterized by steady-state trim conditions, where the aircraft maintains stabilized flight under moderate, non-saturated control inputs. Conversely, throughout phase P7, the controller commands zero thrust while applying maximum pitch rate to induce the rapid attitude modification required for a precise landing flare. Correspondingly, the ground cart acceleration command is driven to its upper bounds from P1 through P4 to rapidly match the aircraft accelerating speed profile. Once kinetic synchronization is achieved, the cart acceleration stabilizes near 0 m/s^2 and remains regulated at this steady state until the end of the mission at physical capture.

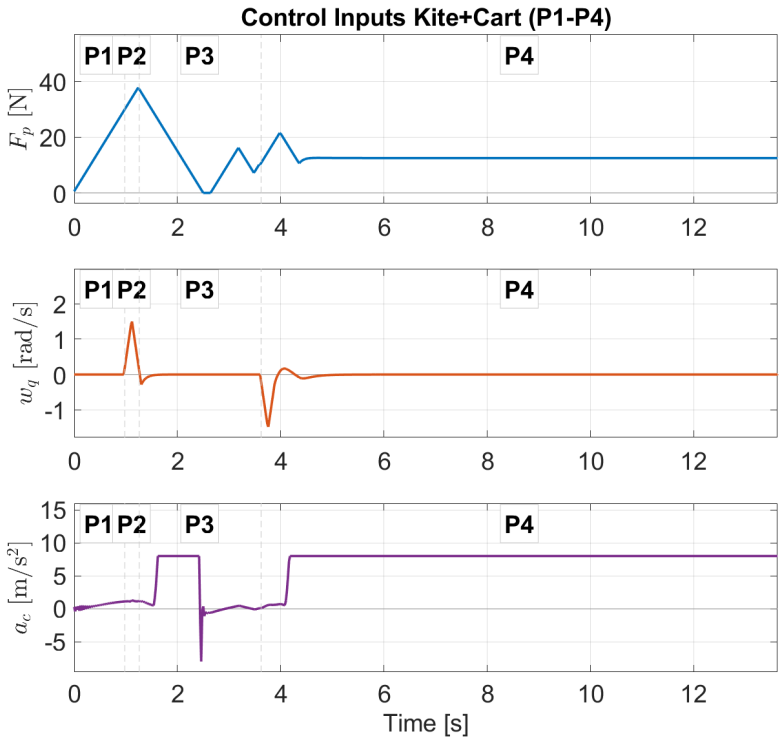

Figure 4.8: Control Inputs Evolution of the Kite-Cart System (P1-P4).

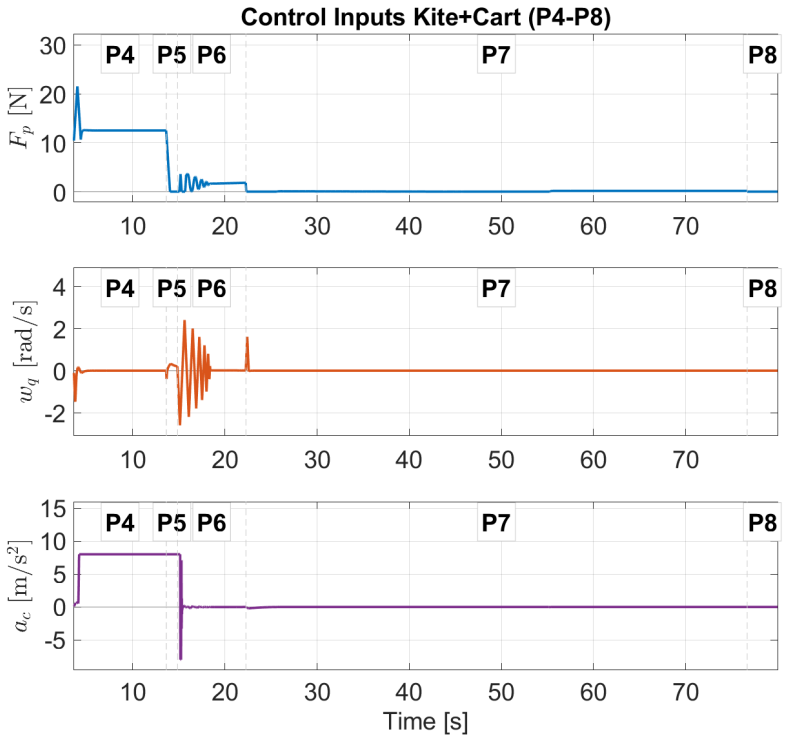

Figure 4.9: Control Inputs Evolution of the Kite-Cart System (P4-P8).

Chapter 5

Hardware Implementation

The theoretical framework developed in Chapter 4 demonstrates a robust synchronization capability within a simulated environment. However, to validate the theoretical results, a physical implementation is required. In this chapter, the physical implementation of the kite-cart system synchronization is presented in detail, Section 5.1 describes the experimental setup, Section 5.2 details the hardware architecture of both kite and cart subsystems, Section 5.3 describes the software implementation executed on each platform, outlining the control loop responsible for processing incoming data and generating the corresponding actuation commands, Section 5.4 presents the experimental validation results, in which the synchronization performance of the carte is compared across several controller gain configurations and, finally, the discussion of the results is performed in Section 5.5.

5.1 Experimental Implementation

The setup consists of the ground-based cart connected via a physical tether to a fixed central anchorage point, forcing it into a constrained circular trajectory with a radius R of approximately 1.4 m. This mechanical constraint physically enforces the circular ground track assumed throughout the kinematic and control formulations of Chapter 4, eliminating the need for an independent lateral guidance mechanism and ensuring that the cart's motion remains confined to a single rotational degree of freedom about the anchorage point. The tether is anchored at a fixed point near the center of the track and routed to one of the lateral sides of the cart, as shown in blue in Figure 5.1, allowing the platform to rotate freely while constraining its radial position. This configuration reproduces the geometric relationship between the kite's tether length and the cart's azimuthal position that underlies the synchronization strategy developed in Section 4.3. The physical experimental platform used to validate the synchronization controller is illustrated in Figure 5.1.

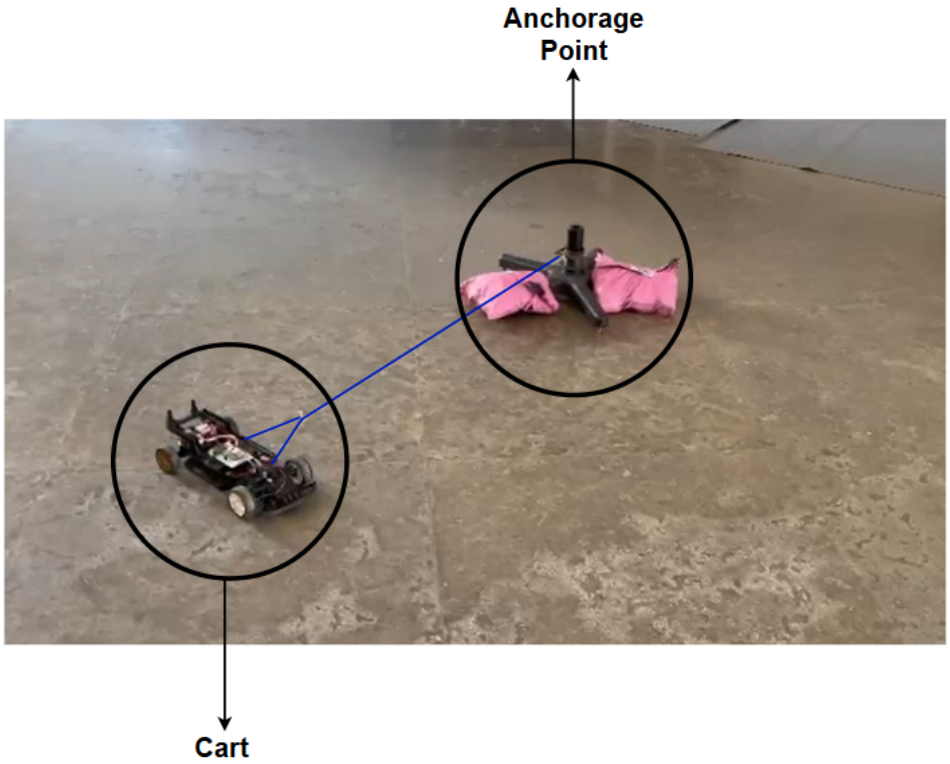

Figure 5.1: Experimental setup showing the tethered cart on the ground connected to the central anchorage point (Tether Highlighted in Blue).

A WiFi communication architecture was developed, utilizing the UDP protocol, established between the kite and the ground cart systems. An Arduino 33 IoT microcontroller onboard, representing the kite, transmits real-time wireless data to a ground-based Raspberry Pi Pico 2W, which acts as the cart controller. This unidirectional communication link delivers two primary states required to apply the control algorithms, namely the kite angular position φ_{kite} and its angular velocity ω_{kite} (Figure 5.2). Since flight testing with a physically flying aircraft was not performed within the scope of this work, the kite's behavior is emulated by a standalone Arduino 33 IoT microcontroller, which generates and transmits synthetic real-time data representative of the expected flight trajectory, in place of a physical onboard unit. This emulation is restricted to the horizontal loitering phase (P4) (Figure 4.1) of the mission, during which the kite's altitude remains fixed. Therefore, vertical dynamics and altitude-dependent maneuvers are outside the scope of the present hardware-in-the-loop validation.

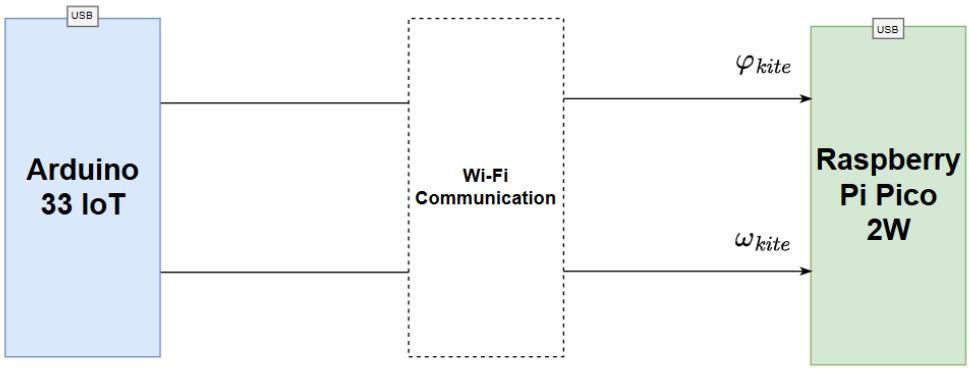

Figure 5.2: WiFi Communication Configuration.

The architecture integrates three primary peripheral modules using dedicated communication buses: an SD card module for local data logging via the Serial Peripheral Interface (SPI) on pins GP10–GP13; a BNO085 Inertial Measurement Unit (IMU) for orientation tracking via the I2C protocol on pins GP20 and GP21; and L298N motor driver for actuation, controlled via GPIO pins GP14, GP15, and GP16, using Pulse-Width Modulation (PWM) and digital logic signals. A common ground is shared across all modules, and a dashed line indicates the 5V logic power routing between the Pico VBUS and the motor driver. Figure 5.3 outlines the hardware schematic and pin configuration of the ground-based cart system, centered around the Raspberry Pi Pico 2W. A battery pack comprising three 3.7V lithium-ion cells connected in series provides a nominal voltage of 11.1V to power the L298N motor driver via its 12V terminal. The positive power rail is routed through a single-pole single-throw (SPST) slide switch to serve as the master hardware toggle for the drive system. A common ground (GND) wire establishes a shared reference plane between the battery pack, the motor driver, and the upstream control electronics.

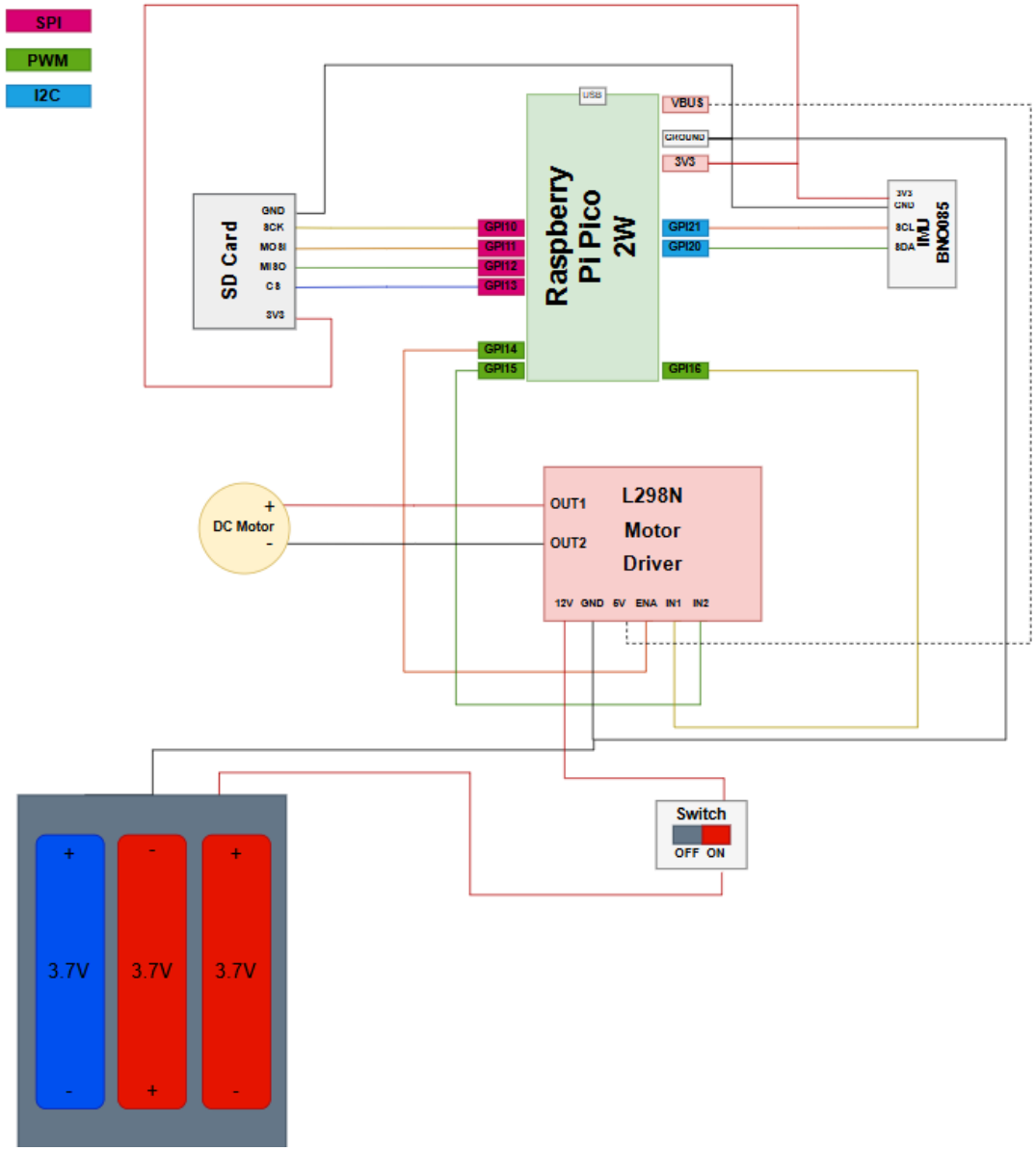

Figure 5.3: Cart Setup Connections.

5.2 Hardware Architecture

5.2.1 Kite Subsystem

A microcontroller was used to emulate the kite subsystem, hosted on a breadboard for testing purposes. Figure 5.4 showcases the Arduino 33 IoT microcontroller used to emulate the kite subsystem, hosted on a breadboard for testing purposes.This setup reflects the pin configuration used to manage the onboard sensors and wireless communication with the ground station, bearing in mind that in the absence of physical flight testing, this hardware operates independently to generate the emulated kite signals described in Section 5.1, rather than being mounted on an actual

aircraft. Figure 5.5 presents the official pinout schematic and multiplexed peripheral functions of the Arduino 33 IoT microcontroller, detailing the board's physical pins and their corresponding hardware capabilities, including power infrastructure, analog inputs, digital input/output (I/O) lines and specialized serial communication buses.

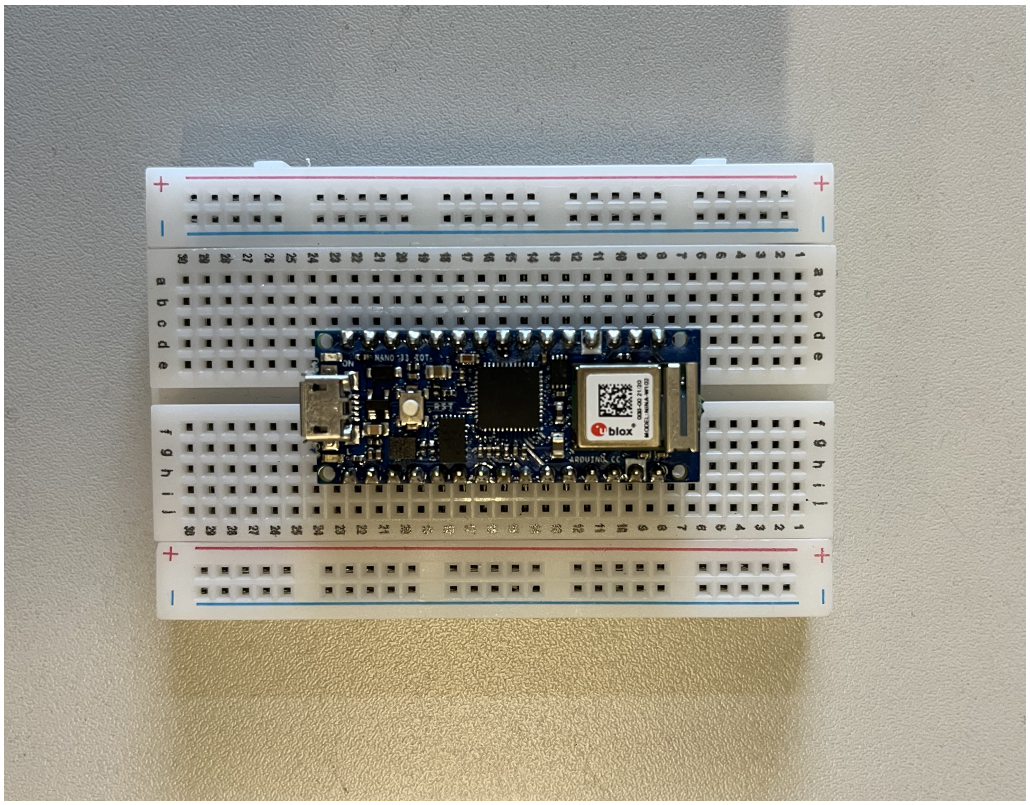

Figure 5.4: Arduino 33 IoT.

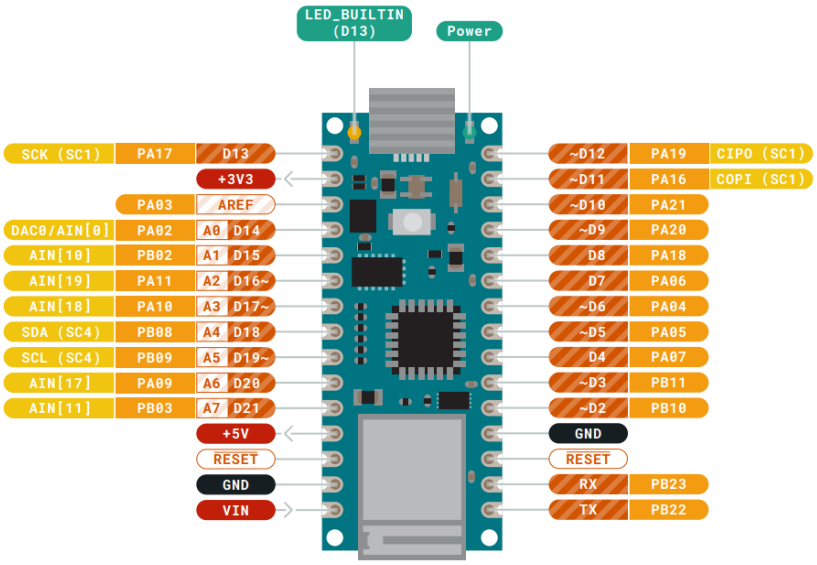

Figure 5.5: Arduino 33 IoT Pinout. (Source: [30])

5.2.2 Cart Subsystem

For the cart subsystem, a Raspberry Pi Pico 2W microcontroller, mounted on a standard breadboard, was used (Figure 5.6). This protoboard configuration serves as the central hardware node for the cart subsystem during the initial prototyping and validation phases.

In Figure 5.7, the official pinout configuration map and multiplexed pin functionalities of the Raspberry Pi Pico 2W microcontroller is illustrated. The color-coded legend classifies the peripheral options available across the board's 40-pin layout, specifying the dedicated channels for power delivery, ground referencing, general-purpose input/output (GPIO), and specialized communication buses. The diagram highlights the pin mappings used by the cart's architecture, including the Serial Peripheral Interface (SPI), Inter-Integrated Circuit (I^2C) and Pulse-Width Modulation (PWM) hardware channels required for simultaneous data logging, orientation tracking and motor control.

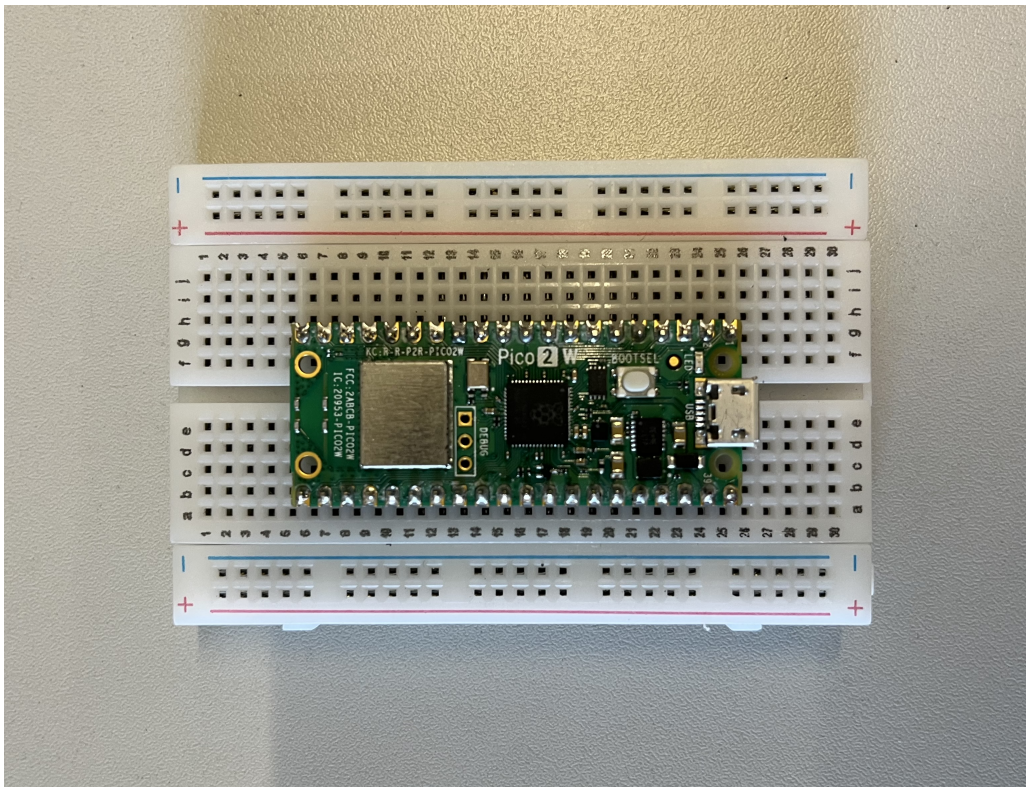

Figure 5.6: Raspberry Pi Pico 2W.

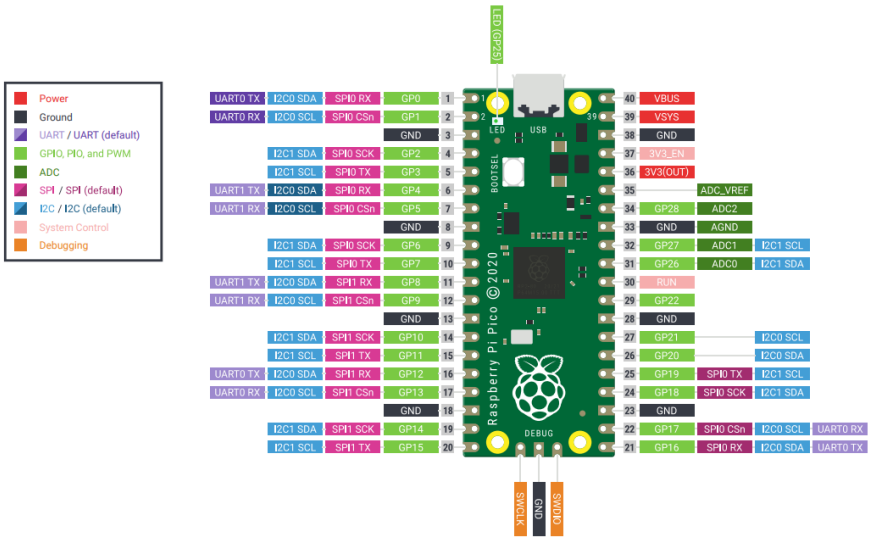

Figure 5.7: Raspberry Pi Pico 2W Pinout. (Source: [31])

In Figure 5.8 the physical BNO085 9 Degree-of-Freedom (9-DoF) Inertial Measurement Unit (IMU) board integrated into the vehicle tracking system is displayed. The module features a standard I2C wiring interface at the bottom edge, using the 3V3, GND, SCL, and SDA pins to com-

municate dynamic orientation data directly to the ground controller. The onboard screen printing details the spatial orientation reference frame (X, Y, and Z axes), which aligns the sensor internal triaxial accelerometer, gyroscope, and magnetometer with the coordinate system of the cart.

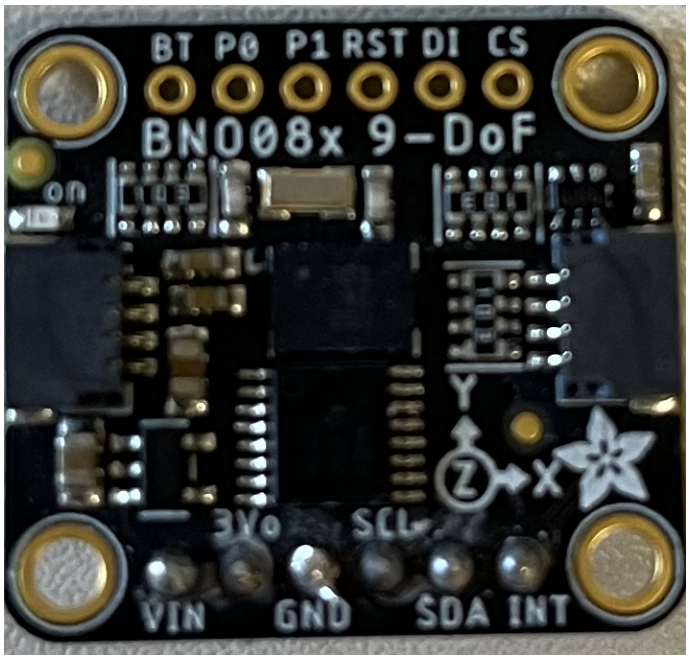

Figure 5.8: IMU BNO085.

Figure 5.9 presents a close-up view of the hardware integration for the local storage subsystem on the cart. A microSD card module containing a 32 GB flash memory card is securely nested within a custom 3D-printed protective enclosure integrated into the cart chassis. The module interface utilizes a 6-pin jumper wire harness to establish the power lines (3.3V and GND) and the Serial Peripheral Interface (SPI) bus communication, comprising the SCK, MOSI, MISO, and CS signals, with the central Raspberry Pi Pico 2W, ensuring data logging during experimental validation.

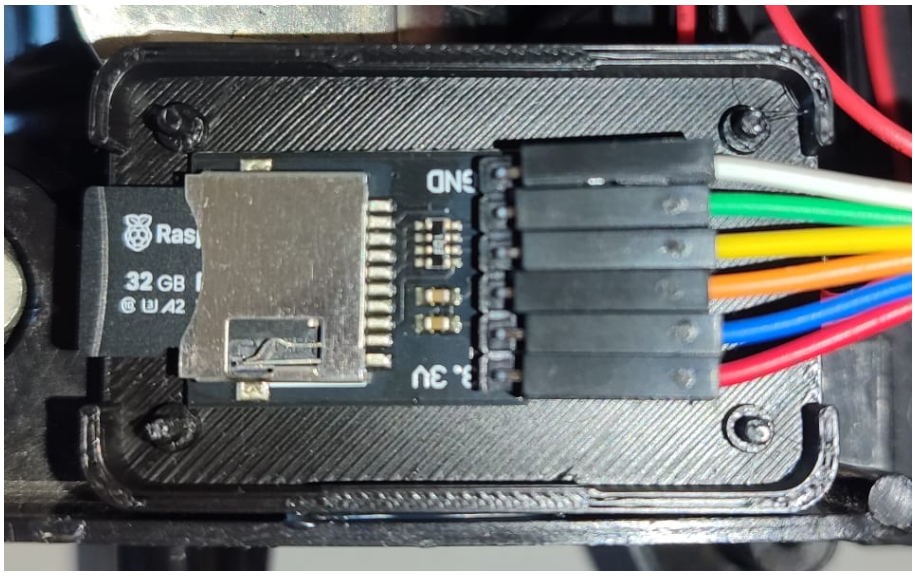

Figure 5.9: MicroSD Card Module for Data Logging.

Figure 5.10 details the physical application and wiring configuration of the L298N dual H-bridge motor driver board integrated into the cart chassis. Since the vehicle operates with a single drive motor, the driver utilizes only the first channel, outputting through OUT 1 and OUT 2, to interface between the battery pack and the motor. The 3-terminal power screw block at the bottom left manages the electrical routing, receiving the main DC supply and establishing a common ground with the logic system. Control signals from the main microcontroller are delivered via a multi-colored jumper wire harness connected to the male header pins at the bottom right.

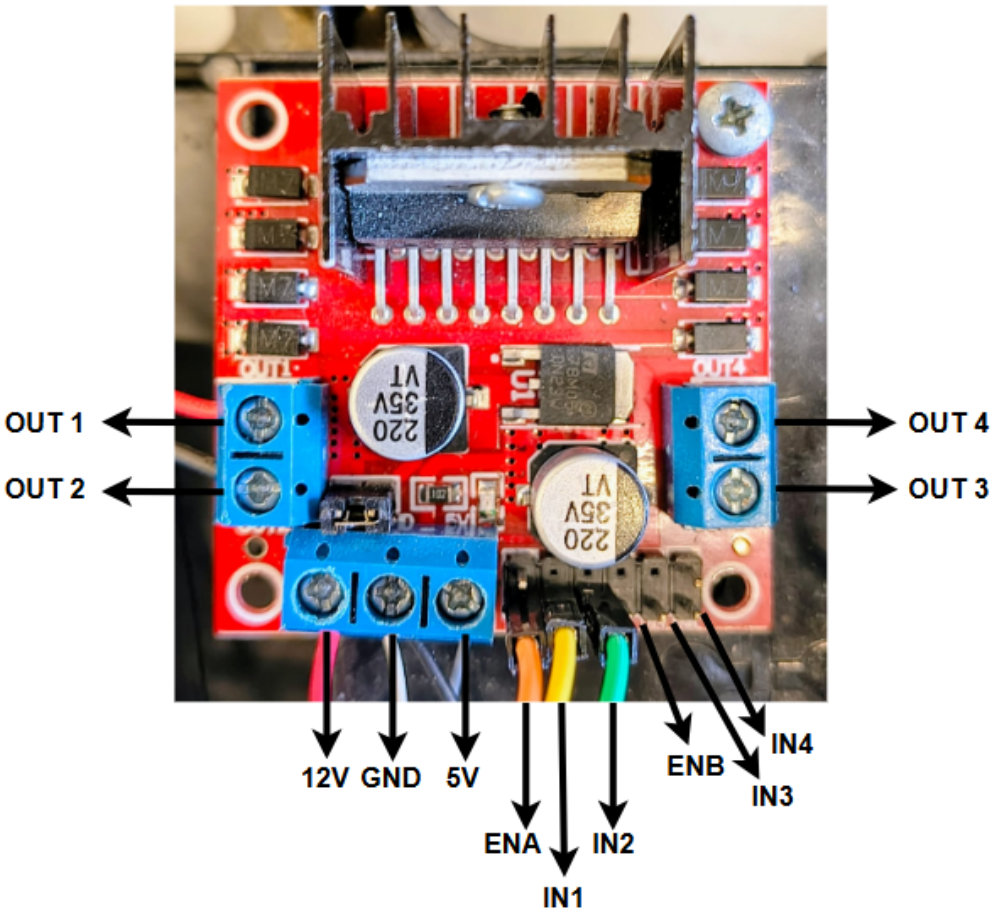

Figure 5.10: L298N Motor Driver. (Source: [32])

Figure 5.11 showcases the physical integration of the cart power supply subsystem within the vehicle chassis. The system is powered by a custom lithium-ion battery pack consisting of three cylindrical cells secured in a dedicated compartment. The batteries, each one providing 3.7 V, are wired in a series configuration to provide a total nominal voltage of 11 V, required by the actuation electronics. The positive and negative power rails, indicated by the red and black wires, respectively, route the current to the switch visible in the upper-left corner of the enclosure, providing a manual safety cut-off point for the entire system.

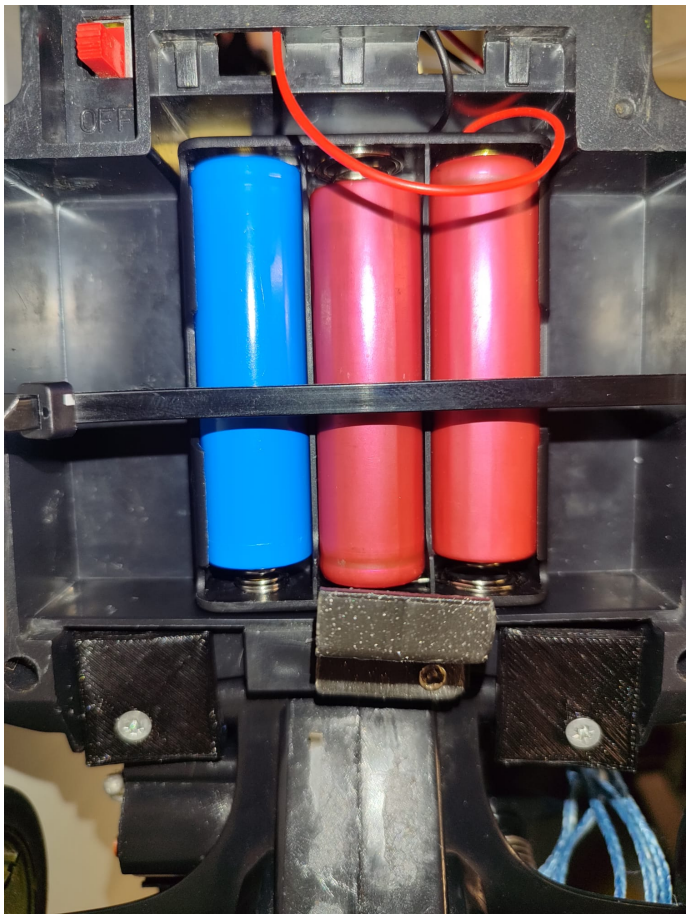

Figure 5.11: Power Supply.

Finally, Figure 5.12 presents the physical experimental setup and hardware implementation of the ground-based cart. The prototype is developed on a mobile wheeled chassis, integrating the electronic modules previously mapped in the schematic diagrams. At the center of the chassis, a breadboard holds the Raspberry Pi Pico 2W controller which coordinates the data acquisition and actuation. The wiring connects the central controller to the local SD card logging module, the red L298N motor driver board responsible for power distribution to the transmission system and the necessary feedback sensors.

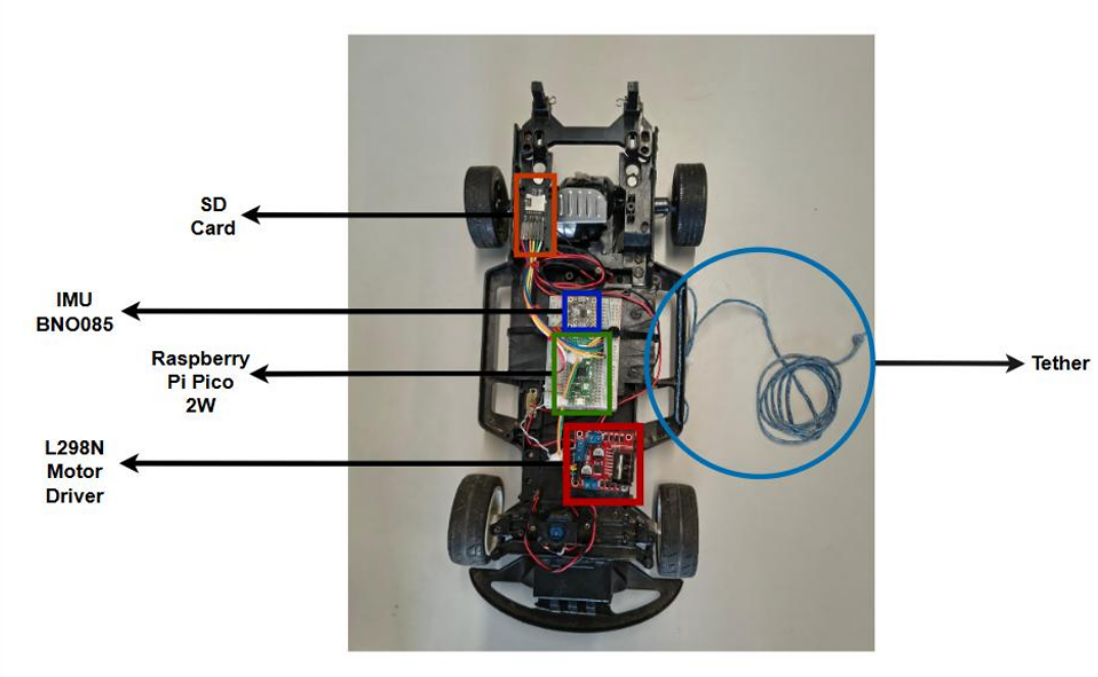

Figure 5.12: Cart Setup.

5.3 Software Implementation

Both Kite Subsystem (Subsection 5.2.1) and Cart Subsystem (Subsection 5.2.2) were developed within the Arduino IDE environment, using C/C++, where the kite-emulation logic is implemented in `speed-controller_RF_WIFI.ino`, while the cart control logic is executed by `cart-subsystem.ino`. Both platforms rely on a shared `wifi_udp_handler.cpp` module to abstract the Wi-Fi/UDP communication layer. Figure 5.13 illustrates the resulting control loop topology executed across the two distributed embedded platforms. On the kite-emulation side, the Arduino 33 IoT executes a fixed-rate execution loop at approximately 50 Hz that integrates the emulated angular position

$$\varphi_{\text{kite}} \mathrel{+}= \omega_{\text{kite}} \Delta t, \tag{5.1}$$

under a constant angular velocity ω_{kite}. The resulting kinematics state is packaged into a lightweight payload via the `buildSensorMessage()` routine and transmitted to the ground cart over Wi-Fi/UDP through `wifi_udp_send()`, while simultaneously being logged to both the Serial monitor interface.

On the cart side, the Raspberry Pi Pico 2W acquires its orientation from the onboard BNO085 IMU (Figure 5.8), converting the sensor's raw quaternion output into a localized yaw angle φ_{cart} via a standard atan2 function implementation. The incoming kite data packet is detected asynchronously using `wifi_udp_has_packet()` and parsed to extract the reference states φ_{kite} and ω_{kite}. As a critical fail-safe measure, a software watchdog mechanism monitors the time elapsed since the last valid transaction: if this timeout interval exceeds 2 s, the firmware raises the

`escKilled` flag and immediately commands a null actuation to the propulsion system, preventing uncontrolled kinetic motion of the cart, in the event of a communication blackout.

When valid telemetry data is available, the cart computes the instantaneous angular phase error $\Delta\varphi$ and the relative angular velocity error between the two systems. It then applies synchronization control law to derive the commanded acceleration a_c, which is dynamically saturated at a structural threshold $a_{c,\max}$. This control output is mapped into a corresponding PWM duty cycle and fed into the L298N motor driver (Figure 5.10) to actuate the cart's DC drive motor. Finally, all synchronized state variables are streamed to `cart_log.csv` on the local SD card (Figure 5.9) for the offline experimental analysis detailed in Section 5.4.

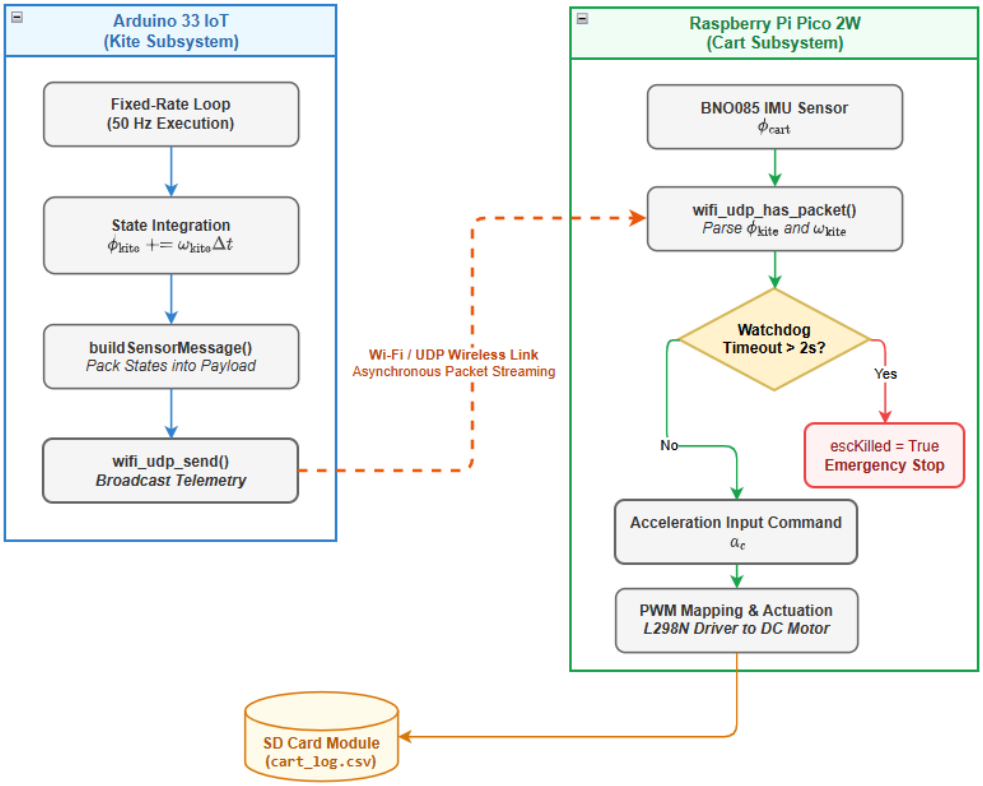

Figure 5.13: Software Implementation Flowchart.

5.4 Experimental Validation

This section presents the experimental validation of the Kite-Cart synchronization controller described in Section 4.3. The validation was performed using data recorded from the cart during circular trajectory tracking tests. For each test, the cart received the angular position of the virtual kite φ_{kite} and its constant angular velocity. The controller then computed the acceleration command and the corresponding ESC signal applied to the cart. The analysis focuses on three main quantities: the angular position of the kite and the cart, the phase error between both systems and

the ESC command signal of the cart. Different gain configurations were tested in order to evaluate their influence on the transient and steady-state response. In order to evaluate the influence of the controller tuning on the synchronization performance, different gain configurations (see Table 5.1) were tested. Each configuration was applied to the same circular trajectory tracking task, allowing the resulting angular tracking error and ESC command behaviour to be compared.

Table 5.1: Controller Gains: All Configurations

Action	**Gain**	**Config. A**	**Config. B**	**Config. C**	**Config. D**
Feedforward	K_f	15.0	15.0	17.0	17.0
Proportional	K_p	16.0	30.0	20.0	35.0
Derivative	K_d	3.5	3.2	3.2	3.2
Integral	K_i	0.5	0.3	0.3	0.3
	$K_{i_{vel}}$	2.3	2.1	2.6	2.6

Configuration A

Configuration A corresponds to the initial gain configuration (see Table 5.2) used during the first experimental test. This configuration was selected as a baseline in order to evaluate the original synchronization behaviour of the cart when tracking the virtual kite trajectory.

Table 5.2: Controller Gains: Configuration A

Action	**Gain**	**Value**
Feedforward	K_f	15.0
Proportional	K_p	16.0
Derivative	K_d	3.5
Integral	K_i	0.5
	$K_{i_{vel}}$	2.3

During the transient response (Figure 5.14), the cart progressively adjusts its angular position to follow the virtual kite trajectory. The angular error decreases continuously, indicating that the controller is able to correct the initial synchronization mismatch. The ESC command remains elevated during this period, showing that significant control effort is required to accelerate the cart and reduce the phase difference. In the steady-state response (Figure 5.15), the system reaches a stable operating condition in which the cart maintains synchronization with the kite trajectory. However, a residual angular error remains, indicating a persistent phase delay between both systems. The ESC signal stabilizes close to its upper operating region, suggesting that the cart operates near its actuation limit to maintain synchronization.

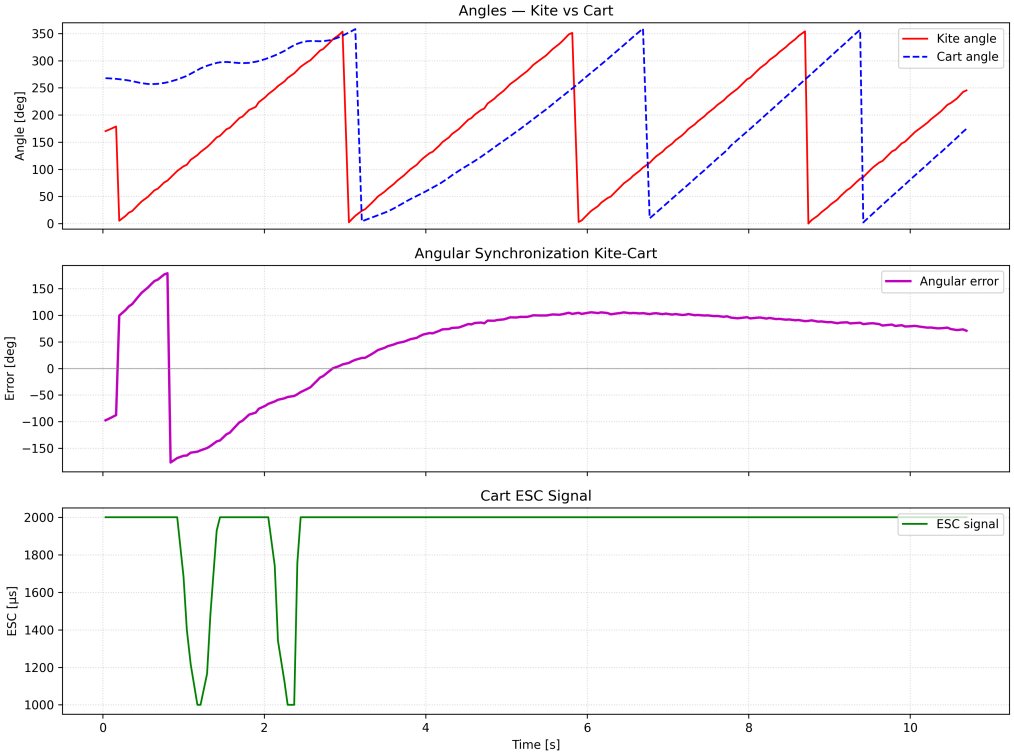

Figure 5.14: Synchronization Results (Transient): Configuration A.

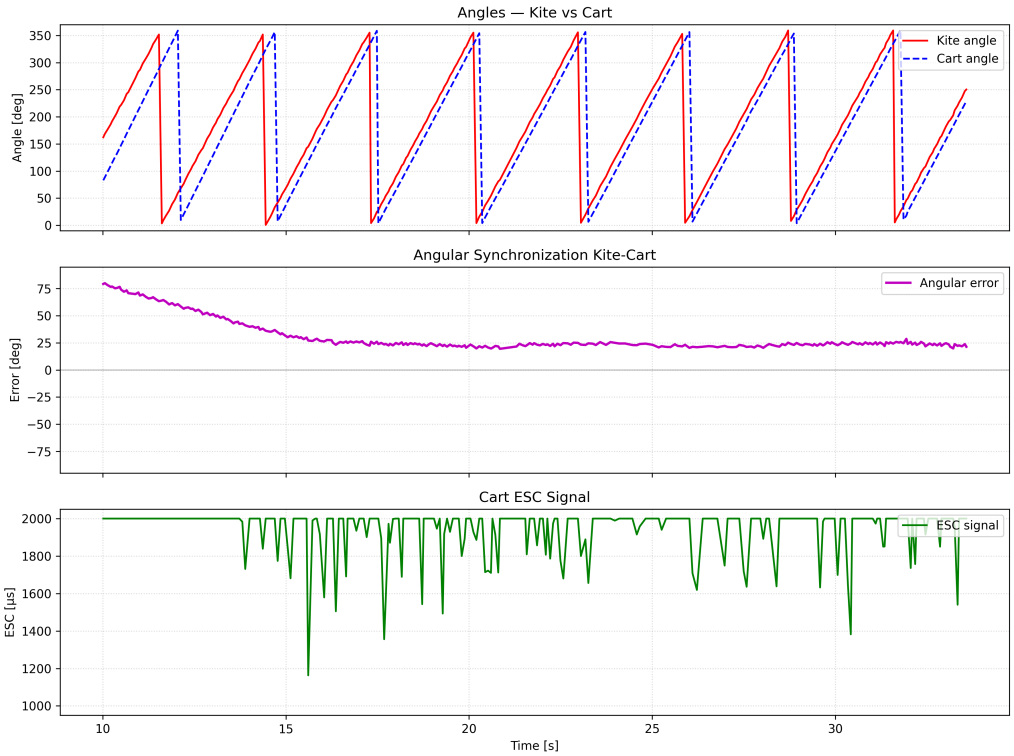

Figure 5.15: Synchronization Results (Steady-State): Configuration A.

Configuration B

Configuration B was defined to evaluate the influence of a higher proportional gain on the synchronization performance. In this configuration (see Table 5.3), the proportional action was intentionally increased in order to obtain a more aggressive correction of the angular error and reduce the phase delay between the kite and the cart. The remaining gains were adjusted to maintain controller stability and limit excessive oscillations or actuator saturation.

Table 5.3: Controller Gains: Configuration B

Action	**Gain**	**Value**
Feedforward	K_f	15.0
Proportional	K_p	30.0
Derivative	K_d	3.0
Integral	K_i	0.3
	$K_{i_{vel}}$	2.1

With the increased proportional gain, the cart reacts more aggressively to the angular error and converges more rapidly toward the kite trajectory. The reduction in phase difference occurs faster than in Configuration A, indicating improved error correction during the transient phase (Figure 5.16). However, the stronger controller action may also lead to larger variations in the ESC command. Once steady-state (Figure 5.17) conditions are reached, the synchronization performance should be evaluated through the residual angular error. A lower final error indicates improved tracking capability, whereas increased oscillatory behaviour may suggest excessive controller aggressiveness. The ESC signal should also be analysed to determine whether the performance improvement requires operation closer to actuator saturation.

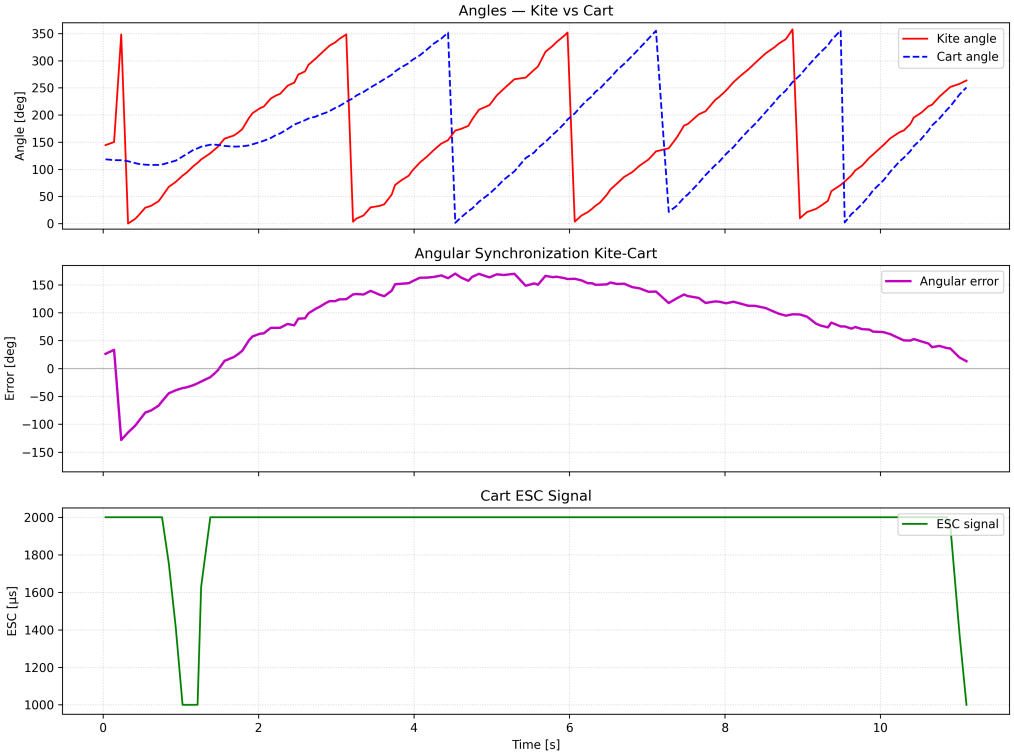

Figure 5.16: Synchronization Results (Transient): Configuration B.

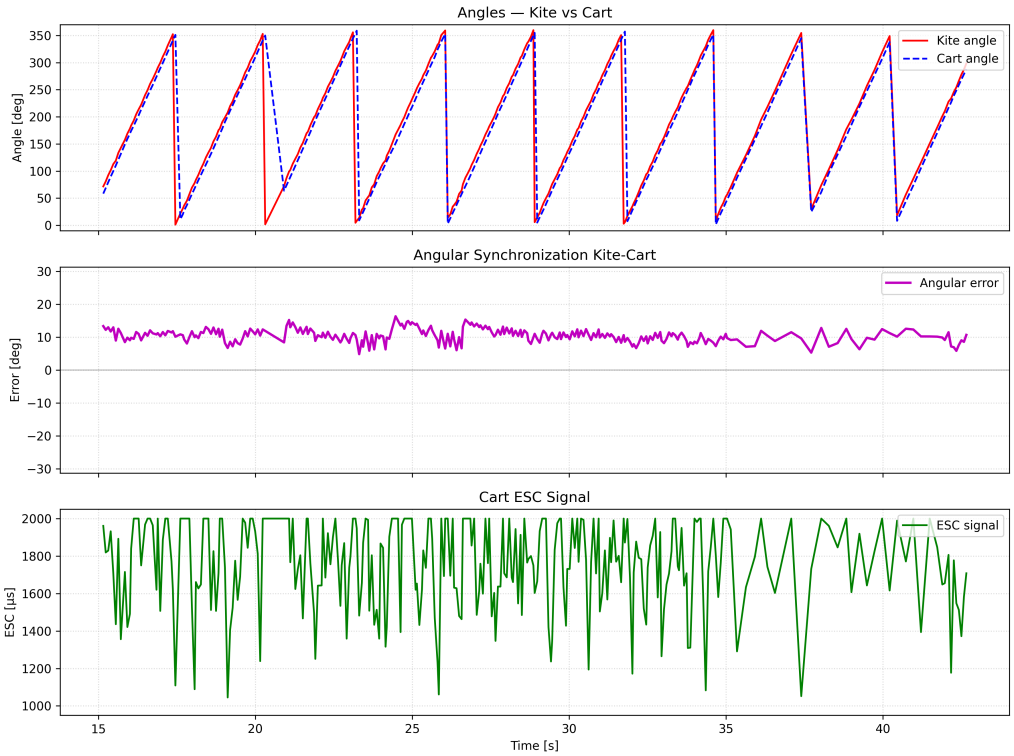

Figure 5.17: Synchronization Results (Steady-State): Configuration B.

Configuration C

Configuration C was designed to investigate whether improving the synchronization performance could be achieved through increased feedforward and velocity-related compensation rather than relying primarily on proportional correction. This configuration (see Table 5.4) aims to improve steady-state tracking while maintaining a smoother control action and reducing excessive ESC saturation.

Table 5.4: Controller Gains: Configuration C

Action	**Gain**	**Value**
Feedforward	K_f	17.0
Proportional	K_p	20.0
Derivative	K_d	3.2
Integral	K_i	0.3
	$K_{i_{vel}}$	2.6

The increased feedforward and velocity-related compensation improve the cart response during the initial synchronization stage (Figure 5.18). The controller anticipates part of the required motion, reducing the dependence on large proportional corrections and producing a smoother convergence toward the kite trajectory. In steady-state operation (Figure 5.19), the effectiveness of the configuration is evaluated by analysing the remaining phase error and the ESC activity, where lower residual error combined with reduced ESC saturation indicates improved synchronization efficiency.

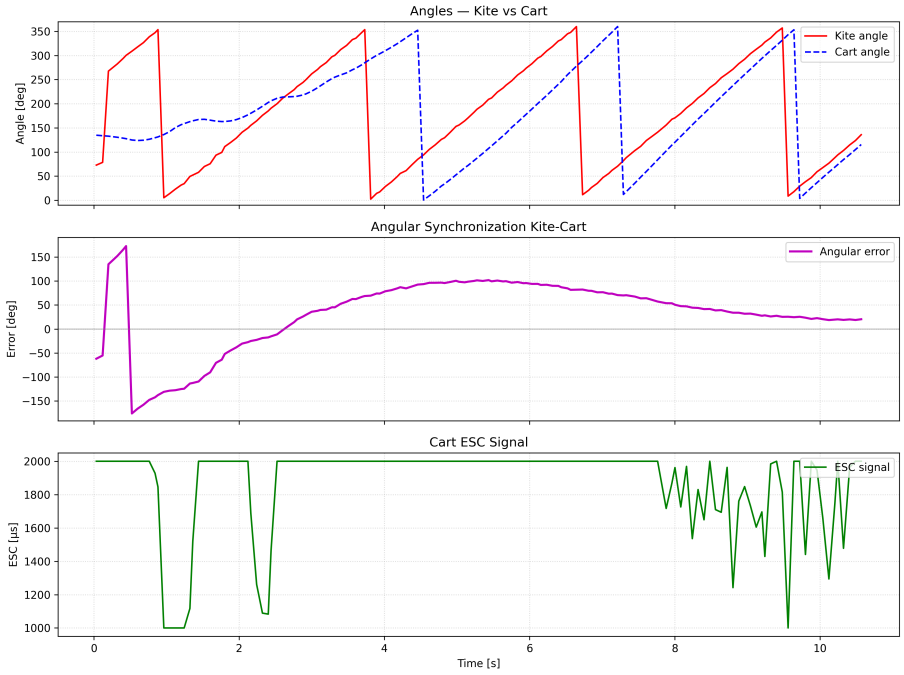

Figure 5.18: Synchronization Results (Transient): Configuration C.

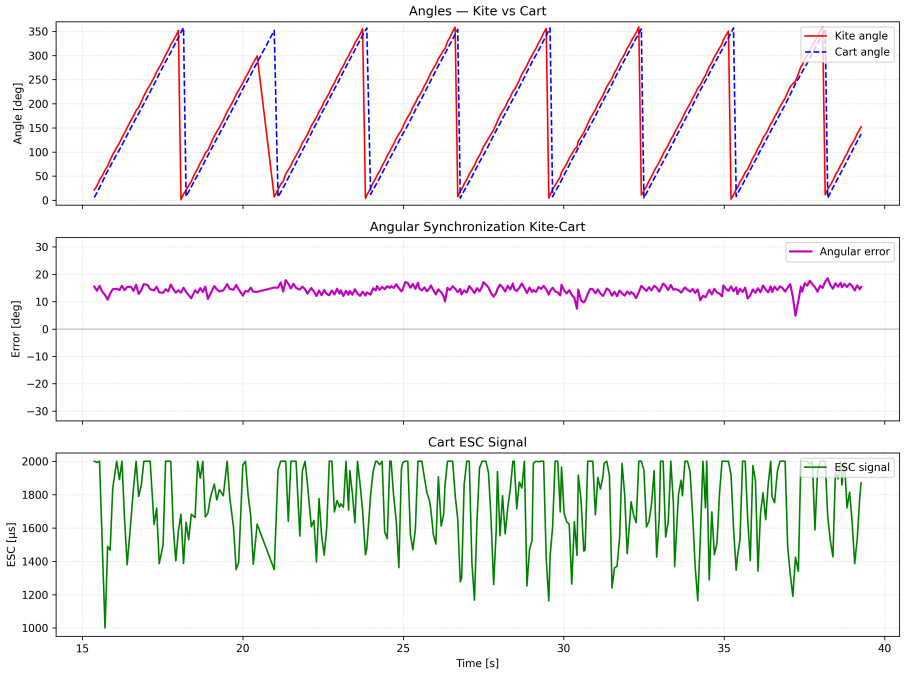

Figure 5.19: Synchronization Results (Steady-State): Configuration C.

Configuration D

Configuration D was defined to evaluate the effect of combining a stronger feedforward action with a higher proportional gain in order to further improve synchronization performance. In this configuration (see Table 5.5), the feedforward gain was increased to provide a higher baseline control action, while the proportional gain was significantly increased to obtain a faster correction of the angular error and reduce the phase delay between the kite and the cart. The derivative and integral gains were maintained at moderate values to preserve controller stability and limit excessive oscillations or error accumulation.

Table 5.5: Controller Gains: Configuration D

Action	Gain	Value
Feedforward	K_f	17.0
Proportional	K_p	35.0
Derivative	K_d	3.2
Integral	K_i	0.3
	$K_{i_{vel}}$	2.6

The combination of increased feedforward and proportional gains produces a more aggressive synchronization behaviour during the transient phase (Figure 5.20). The cart responds more rapidly to angular deviations and attempts to reduce the phase difference in a shorter time interval. This behaviour may result in larger ESC variations and stronger control effort. After convergence

(Figure 5.21), the synchronization quality is determined by the remaining angular offset and the required ESC command. If the residual error decreases relative to previous configurations, the tuning can be considered beneficial. If the ESC remains close to saturation or oscillatory behaviour appears, the gains may exceed the practical operating limits of the cart.

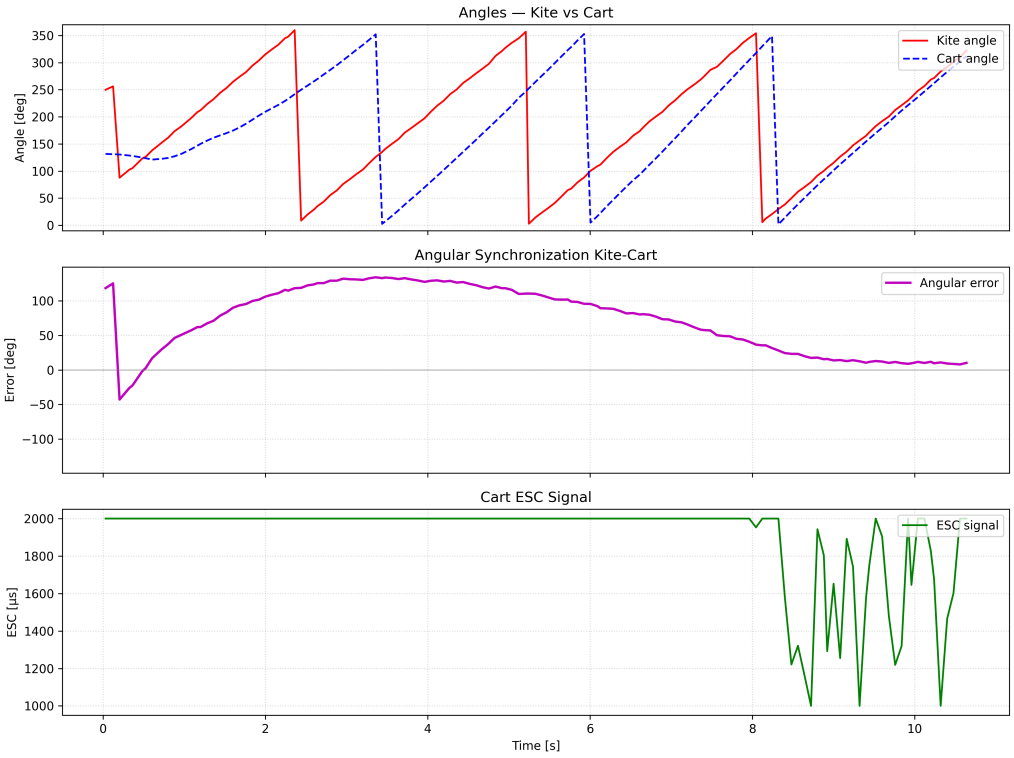

Figure 5.20: Synchronization Results (Transient): Configuration D.

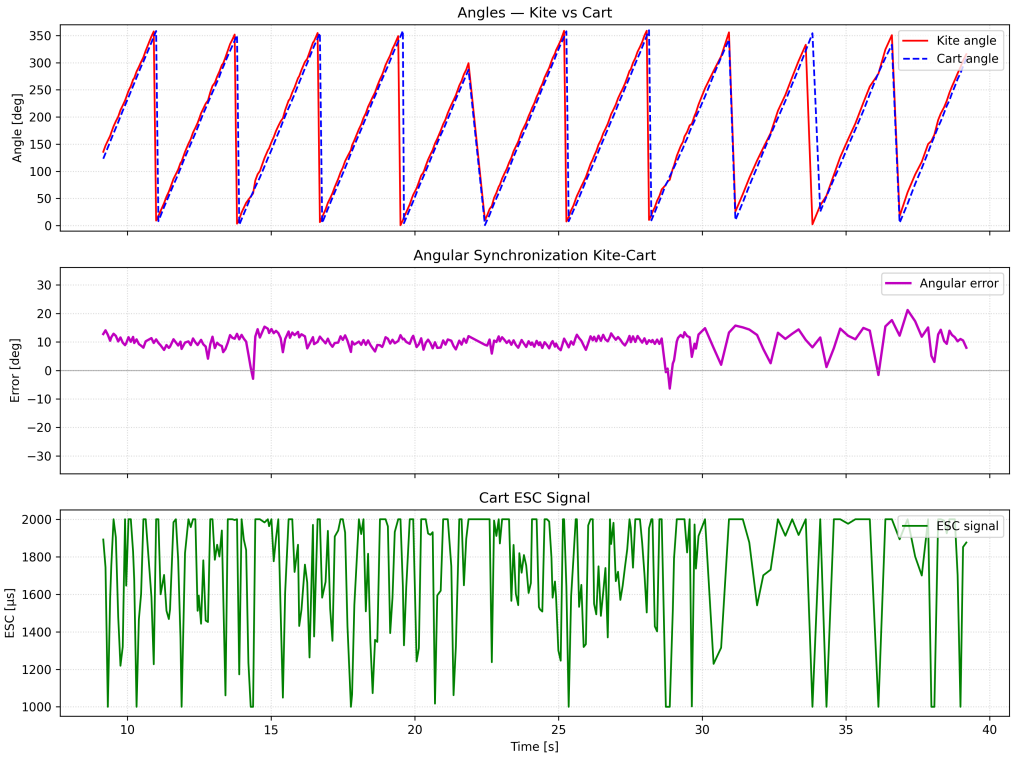

Figure 5.21: Synchronization Results (Steady-State): Configuration D.

5.5 Discussion

The experimental validation results demonstrate that the proposed synchronization controller effectively drives the cart to follow the angular trajectory imposed by the virtual kite across all tested gain configurations. However, the experiments also reveal that controller tuning significantly influences both synchronization quality and control effort.

Configuration A provided a stable baseline behavior, demonstrating the effectiveness of the synchronization strategy under nominal conditions. During the transient phase, the cart progressively reduced the initial phase difference, ultimately reaching a stable operating condition. Nevertheless, a residual angular error persisted during steady-state operation, indicating that the cart was unable to completely eliminate the phase delay relative to the kite.

Configuration B introduced a higher proportional gain. The experimental results showed that increasing the proportional action enhances transient convergence and accelerates the approach to the kite's trajectory. However, this improvement was accompanied by a more demanding ESC command, reflecting increased actuator effort. Although the angular error decreased, excessive proportional action elevates sensitivity to disturbances and risks driving the actuator toward saturation.

Configuration C explored an alternative tuning strategy by increasing feedforward and velocity-related compensation instead of relying primarily on proportional feedback. This configuration

aimed to enhance synchronization while maintaining a smoother control action. The results suggest that anticipating the required motion reduces reliance on large feedback corrections and improves steady-state tracking behavior.

Configuration D combined increased feedforward and proportional gains. This configuration yielded the most aggressive controller response, allowing for an evaluation of the kite-cart system practical limits. While higher gains can mitigate phase delay, the experimental results indicate that improvements in synchronization are ultimately constrained by the physical capabilities of the cart and the operational range of the ESC.

Across all tested configurations, the angular error consistently decreased during the transient phase and converged to a bounded value during steady-state operation, thereby demonstrating stability. A complete elimination of the phase offset was not always achieved. This behavior suggests that synchronization performance is governed not only by controller tuning but also by inherent physical constraints, such as actuator limitations, communication delays and the maximum achievable cart velocity. Consequently, the experimental outcomes reveal that increasing controller aggressiveness does not yield a proportional improvement in synchronization accuracy. The optimal performance is achieved by balancing rapid error correction with moderate actuator effort, thereby avoiding prolonged ESC saturation.

Another critical factor influencing the experimental outcomes is the tether length constraint. Since the cart follows a circular trajectory with a fixed radius, the required linear velocity increases proportionally with the imposed angular velocity of the virtual kite. A portion of the steady-state angular delay observed in certain configurations may be attributed to the cart reaching its physical speed limit rather than to insufficient controller gains. This hypothesis is supported by the ESC behavior, which frequently approached its upper operating limit during synchronization. Therefore, further increases in controller aggressiveness are incapable of eliminating the residual angular error if the required cart velocity exceeds the physical capabilities of the system.

Chapter 6

Conclusion

This document addressed a key challenge in the development of AWES: bridging the gap between theoretical power generation concepts and fully autonomous operation. The operational viability of AWES project depends largely on the successful automation of take-off and landing procedures. To support this objective, this work established a comprehensive framework for the development of a CTOL platform. The work began with a review of the AWES State-of-the-Art and a technical characterization of the small-scale aircraft prototype, followed by the kinematic and dynamic modelling of the kite–cart system. Based on this analysis, a hierarchical control architecture was developed, combining phase-specific PID/LQR control laws with a synchronization strategy to coordinate the autonomous cart with the aircraft circular trajectory across the different mission phases. The proposed synchronization and capture strategy was initially assessed through numerical simulation in MATLAB, where the controller demonstrated the ability to track the kite trajectory and progressively reduce angular and velocity tracking errors to levels compatible with autonomous capture requirements. To move beyond simulation and bring the control framework closer to a realistic implementation, a physical prototype of the ground cart was developed using a Raspberry Pi Pico 2W controller and experimentally validated through a hardware-in-the-loop setup.

In this experimental platform, an Arduino Nano 33 IoT emulated the aircraft and transmitted synthetic real-time position and orientation data through a wireless communication link, reproducing the expected aircraft behaviour during the constant-altitude loitering phase. This approach enabled validation of the embedded control system under realistic timing, synchronization and communication constraints without requiring a flight-capable aircraft. The experimental results demonstrated that the proposed architecture is capable of achieving stable synchronization between the cart and the aircraft trajectory while highlighting practical limitations associated with actuator capability, synchronization delays and the physical constraints imposed by the tethered configuration. These observations provide valuable insight into the requirements for future real-world implementation. Although full validation with a physically flying aircraft was outside the scope of this work, the results obtained through simulation and hardware-in-the-loop experimentation establish a solid foundation for the continuation of the project. Overall, the developed ATOL

platform represents a meaningful step toward autonomous airborne wind energy operation and provides the necessary groundwork for future integration with a real flight-capable aircraft and a complete autonomous landing sequence.

6.1 Future Work

Several directions remain open for future development. The most immediate priority is the integration and experimental validation of the system with a physically flying aircraft, replacing the emulated Arduino-based kite used in the current hardware-in-the-loop tests. This would enable the synchronization and capture strategy to be evaluated under real operating conditions, including aerodynamic disturbances, sensor noise, communication latency, which cannot be fully reproduced in simulation or emulation and would extend the experimental validation beyond the loitering phase to cover the complete mission sequence.

Another important aspect concerns the physical limitations identified during the synchronization experiments. In the current implementation, the cart motion is constrained by the tether length, which directly affects the linear velocity required to maintain angular synchronization with the aircraft. Future work should investigate the influence of tether geometry and length on synchronization performance and evaluate adaptive strategies capable of compensating for these physical constraints during landing. A related direction concerns the physical capture mechanism itself. The current implementation relies on synchronizing the cart with the aircraft azimuthal position while maintaining the kite at approximately constant altitude, without a dedicated mechanism to physically secure the aircraft after touchdown. Introducing an active capture mechanism, such as magnetic coupling integrated into the cart platform, remains a promising direction for future work. Such a system could enable the transition from trajectory synchronization alone to a fully ATOL sequence. Finally, future developments may focus on evaluating the robustness of the proposed control architecture under varying wind conditions, improving tolerance to timing and positioning uncertainties during landing and extending the synchronization strategy to multi-kite scenarios, as proposed within the broader UPWIND research roadmap.

References

[1] *THE 17 GOALS | Sustainable Development*. URL: https://sdgs.un.org/goals (visited on 12/15/2025).

[2] Mahdi Ebrahimi Salari, Joseph Coleman, and Daniel Toal. "Airborne Wind Energy—A Review". en. In: *3rd International Congress on Energy Efficiency and Energy Related Materials (ENEFM2015)*. Ed. by Ahmet Yavuz Oral and Zehra Banu Bahsi Oral. Series Title: Springer Proceedings in Energy. Cham: Springer International Publishing, 2017, pp. 81–92. ISBN: 978-3-319-45676-8 978-3-319-45677-5. DOI: 10.1007/978-3-319-45677-5_10.

[3] Antonello Cherubini et al. "Airborne Wind Energy Systems: A review of the technologies". en. In: *Renewable and Sustainable Energy Reviews* 51 (Nov. 2015), pp. 1461–1476. ISSN: 13640321. DOI: 10.1016/j.rser.2015.07.053.

[4] Gabriel M. Fernandes. "Take-off and landing of autonomous flying wings in airborne wind energy systems." en. MA thesis. University of Porto, 2023.

[5] *UPWIND Project*. en. URL: https://www.upwindresearchproject.com (visited on 12/27/2025).

[6] João Pedro Martinho Legoinha. "UPWIND Master Thesis - Take-off and Landing with an Auxiliary Vehicle of an Autonomous Wing in Airborne Wind Energy Systems". en. MA thesis. University of Porto, 2025.

[7] *17TH APCA International Conference On Automatic Control And Soft Computing*. URL: https://controlo2026.apca.pt/ (visited on 06/30/2026).

[8] Roland Schmehl. *Airborne Wind Energy*. en-us. June 2019. URL: http://awesco.eu/awe-explained/ (visited on 12/15/2025).

[9] Ana Rita Reimão Couto. "UPWIND - Pendulum-Based Take-off for Autonomous Flying Wings in Airborne Wind Energy Systems". en. MA thesis. University of Porto.

[10] Moritz Diehl. "Airborne Wind Energy: Basic Concepts and Physical Foundations". en. In: *Airborne Wind Energy*. Ed. by Uwe Ahrens, Moritz Diehl, and Roland Schmehl. Series Title: Green Energy and Technology. Berlin, Heidelberg: Springer Berlin Heidelberg, 2013, pp. 3–22. ISBN: 978-3-642-39964-0 978-3-642-39965-7. DOI: 10.1007/978-3-642-39965-7_1.

[11] *Airborne Wind Energy Conference 2026 (AWEC 2026)*. 2026. URL: https://awec2026.com/ (visited on 06/27/2026).

[12] *Airborne Wind Energy 2025/2026*. URL: https://awecourse.github.io/slides/ (visited on 03/19/2026).

[13] M. L. Loyd. "Crosswind kite power". In: *Journal of Energy* 4 (June 1980), pp. 106–111. DOI: 10.2514/3.48021.

[14] Philip Bechtle et al. *AWEsome: An open-source test platform for airborne wind energy systems*. en. arXiv:1704.08695 [eess]. Apr. 2017. DOI: 10.48550/arXiv.1704.08695.

[15] *AWE systems | Airbornewindeurope*. en-US. URL: https://airbornewindeurope.org/awe-systems (visited on 06/20/2026).

[16] Jochem Weber et al. "Airborne Wind Energy". en. In: *Renewable Energy* (Aug. 2021). DOI: 10.2172/1813974.

[17] Lorenzo Fagiano et al. "Autonomous Airborne Wind Energy Systems: Accomplishments and Challenges". en. In: *Annual Review of Control, Robotics, and Autonomous Systems* 5.1 (May 2022), pp. 603–631. ISSN: 2573-5144, 2573-5144. DOI: 10.1146/annurev-control-042820-124658.

[18] Sérgio Vinha et al. "Automatic Circular Take-off and Landing of Motorized Tethered Aircraft". en. In: *2024 European Control Conference (ECC)*. Stockholm, Sweden: IEEE, June 2024, pp. 681–686. ISBN: 978-3-907144-10-7. DOI: 10.23919/ECC64448.2024.10590893.

[19] Sérgio Vinha, Gabriel Fernandes, and Fernando Fontes A.C.C. "A Discussion on Automatic Take-off and Landing Approaches for Airborne Wind Energy Systems". In: *AWEC 2024 - Airborne Wind Energy Conference*. Madrid, Spain, 2024. URL: https://awec2024.com/images/posters/AWEC2024_poster_Sergio_Vinha.pdf (visited on 12/22/2025).

[20] *Makani - A Google X Moonshot*. URL: https://x.company/projects/makani/ (visited on 12/22/2025).

[21] *Introducing the KM2 system*. URL: https://www.kitemill.com/news/introducing-the-km2-system (visited on 12/22/2025).

[22] *TwingTec*. en-GB. URL: https://twingtec.ch/ (visited on 12/22/2025).

[23] Uwe Ahrens. *Airborne Wind Energy: An Overview of the Technological Approaches*. Green Energy and Technology. Springer Cham, Nov. 2022. ISBN: 978-3-031-19953-0. DOI: https://doi.org/10.1007/978-3-031-19954-7.

[24] Author richard94501. *Google wind energy kite nears launch date*. en. Oct. 2015. URL: https://alamedapointenviro.com/2015/10/08/google-wind-energy-kite-nears-launch-date/ (visited on 12/22/2025).

[25] André F. C. Pereira and João M. M. Sousa. "A Review on Crosswind Airborne Wind Energy Systems: Key Factors for a Design Choice". en. In: *Energies* 16.1 (Dec. 2022), p. 351. ISSN: 1996-1073. DOI: 10.3390/en16010351.

[26] *ElektRail*. de. URL: https://elektrail.com/ (visited on 12/26/2025).

[27] Johannes Müller, Mostafa Elhashash, and Volker Gollnick. "Electrical Launch Catapult and Landing Decelerator for Fixed-Wing Airborne Wind Energy Systems". en. In: *Energies* 15.7 (Mar. 2022), p. 2502. ISSN: 1996-1073. DOI: 10.3390/en15072502.

[28] Randal Beard W. and Timothy McLain W. *Small Unnamed Aircraft*. en. Oct. 2025.

[29] Luís Paiva and Fernando Fontes. "Optimal Control Algorithms with Adaptive Time-Mesh Refinement for Kite Power Systems". en. In: *Energies* 11.3 (Feb. 2018), p. 475. ISSN: 1996-1073. DOI: 10.3390/en11030475.

[30] *Arduino 33 IoT Pinout*. URL: https://docs.arduino.cc/resources/pinouts/ABX00027-full-pinout.pdf (visited on 06/09/2026).

[31] *RP-008309-DS-1-Pico-R3-A4-Pinout*. URL: https://pip-assets.raspberrypi.com/categories/610-raspberry-pi-pico/documents/RP-008309-DS-1-Pico-R3-A4-Pinout.pdf (visited on 06/09/2026).

[32] *L298N Motor Driver*. URL: https://www.handsontec.com/dataspecs/L298N%20Motor%20Driver.pdf (visited on 06/09/2026).